An investigation into self assembled super-lattices of strongly correlated adatoms on metallic surfaces through

Blackbourn, David James

Awarding institution:
King's College London

An investigation into self assembled super-lattices of strongly correlated adatoms on metallic surfaces through the use of Dynamical Mean Field Theory

By David James Blackbourn

Supervised by Dr Cédric Weber

A thesis presented on September 30th 2016 as part fulfilment of the conditions required for the awarding of the title and degree of

Doctor of Physics

Department of Physics
King's College London
United Kingdom
2016

Abstract

We use dynamical mean field theory to investigate the nature of self assembled super-lattices of strong correlated adatoms on metallic surfaces, motivated by the realisation of a Ce super-lattice on an Ag(111) surface, which invites interest as a significant step in our understanding and manipulation of complex nano-scale systems and in the development of technological applications such as atomic scale memory devices.

We build upon previous tight binding studies by using the Anderson impurity model to describe a collection of one band strongly correlated impurities on a surface, which exhibit an on-site Coulomb repulsion U when doubly occupied and can hybridise with the adsorbed surface states. We set out the DMFT framework used, explaining how we employ the Hubbard 1 approximation and exact diagonalisation impurity solvers to self consistently include the strong Hubbard U interaction. We discuss the mathematical methods used in the course of our calculations and the computational techniques which make our simulations more time and memory efficient.

Our results explore the effect that changing numerous model parameters such as U, total electron density and adatom separation has on several impurity quantities, including occupation, magnetic moment and effective mass/Z function. We consider spectral functions and band structures to gain insight into changes in system behaviour due to these variations. We find that the system contains many competing interactions which produce a complex array of phenomena.

We conclude that our work gives insight into the behaviour of self assembled super-lattices, suggesting the inclusion of U is important for understanding the rarity of such systems. We discuss the myriad ways in which this topic should be further studied and outline the future work to be done in improving this method and applying it to diverse problems such as disorder and cluster effects such as RKKY.

Acknowledgements

I would like to thank first and foremost my supervisor Cédric. Your guidance and support has allowed me to produce this work and I will always appreciate everything you have taught me. Thank you for giving me the opportunity to learn and earn this achievement.

Secondly, thank you to my thesis examiners, Stewart and Giovanni. You helped make the viva a much more pleasant experience than I imagined it could be and gave invaluable advice to help make this record of my work the best it could be.

Finally, I am more grateful than I can ever express to my friends, family and Lauren, for always believing that I was capable of achieving this even when I doubted it, and without whom I never would have.

Contents

List of Figures

List of Tables

Part I

Preliminaries

Chapter 1

Introduction

1.1 Motivations

In this report we present progress into the study of self assembly mechanisms in the case of adatom super-lattice self formation on metallic surfaces, in particular motivated by previous experiments showing the self organisation of randomly deposited Ce on an Ag(111) surface state [1], which can be seen in Fig. 1.1.

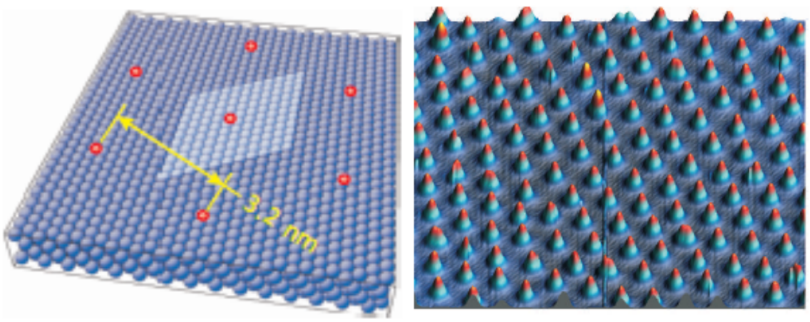

Figure 1.1: Left: A schematic representation of Ce adatoms (red) lying in a lattice formation upon the Ag(111) surface (blue). The lighter blue area denotes the unit cell upon which a Tight Binding calculation was carried out. Noted on it is the observed and predicted adatom distance of 3.2 nm. Right: An STM image of the observed Ce super-lattice, at 3.9 K. Images borrowed from [1] and the subsequent poster from this work and [2]

Our investigation is motivated by the fact that systems such as these are not only deserving of academic attention but offer real applicability and opportunity for technological innovation. In particular, the fact that systems which exhibit self assembly mechanisms are quite rare and are borne out of a complex dynamic between multiple interactions make them quite clearly fascinating from a purely intellectual perspective. But what is also clear if that they offer the possibility of a significant shift in our methods of technology manufacture, being the basis by which current 'top down' techniques could be replaced by the 'bottom up' approach, which brings with it many advantages and improvements.

Predominantly, self organising structures like Ce/Ag(111) offer an attractive alternative to the current techniques of manually ordering systems, such as through manipulation of atomic positions using an STM tip. For example, the latter manual process has been employed by IBM [10] in the pursuit of atomic scale memory storage. If we consider the present state of magnetic memory technology, it becomes quite obvious how the introduction of self assembly behaviour could herald a vast improvement in functionality.

Current magnetic memory storage devices, such as hard disk drives, store binary data as magnetic moments across a surface, with the "up" and "down" orientation of these moments corresponding to the binary digits, 1 and 0. On a ferromagnetic surface, as used in these devices, the correlation between electrons makes it favourable for large numbers of them to have the same magnetic orientation. This means that these "up" and "down"

orientated areas have relatively large spatial dimensions containing many electrons, which limits the data resolution of the device. This is however a bonus in the case of reading the information back - a larger field strength is required for the read/write head to detect it.

If we were to shrink the area over which a single binary digit could be stored and detected then correspondingly more bits could be recorded within a device, with the culmination and ultimate goal of such efforts being information storage at the atomic level. To this end, work done by IBM [10] has shown that through using an STM to manually place Fe adatoms in an anti-ferromagnetic arrangement on a Cu surface, data can be stored with much greater spatial resolution. An example is shown below in Fig. 1.2, where at low temperatures a single bit could be stored with as little as 12 atoms.

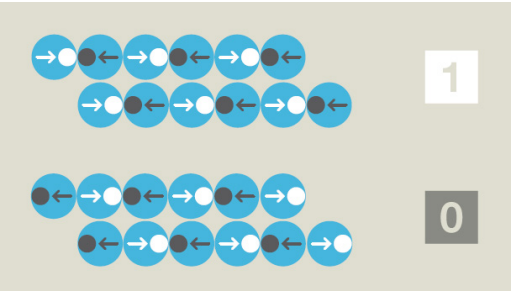

Figure 1.2: Schematic of the IBM experiment, showing how at low temperatures a single binary digit could be stored with 12 atoms. Image taken from the IBM website [3].

However the important distinction is that with the self assembly behaviour we have studied through numerical simulations and a theoretical framework, there exists the possibility of achieving such success without

the need for direct manipulation, but rather through tuning of physical parameters to create the atomic scale structures desired.

There has also been interest in atomic scale memory storage more recently, with a paper being released demonstrating how a kilobyte of rewriteable memory has been stored using Cl vacancies on Cu(100) [11]. This makes use of its own self assembly mechanism [12], where Cl form a lattice on the surface within which they can be moved using an STM tip. This differs from the mechanism we investigate as this is not a dilute super-lattice, the Cl occupy adjacent sites on top the substrate and so any information must necessarily be stored with position. Dilute super-lattices however offer the prospect of encoding with magnetic moments, with it being feasible that distinct and independent moments could be recorded using small clusters or even individual adatoms, meaning a greatly increased data capacity.

Clearly the technological ramifications of self assembled super-lattices could go far beyond just the possibility discussed. This simply serves to illustrate that there is significant motivation to study these systems from an application standpoint in addition to intellectual curiosity, which has driven previous research in the field and which we also hope to inspire with our work.

1.2 Review of previous studies

As previously stated our investigation is chiefly motivated by the study outlined in Ref. [1], but this discovery came as the culmination of decades of study into the behaviour of adatoms on surfaces. In the following sections we will give an overview of this body of work, beginning with the understanding and description of long range surface-mediated interactions between adatoms and how this can lead to self assembly in a variety of systems. We then discuss in greater detail the theoretical and experimental work done regarding the Ce/Ag(111) super-lattice, which explains the system in terms of a tight binding model.

1.2.1 Long Range Adatom Interactions

Long range effects between adatoms on surfaces are well established phenomena both theoretically and experimentally, with Lau and Kohn [13] describing the indirect oscillatory interaction between adsorbed atoms mathematically in 1978, after previous discussions and experimental evidence [14] [15] [16] [17].

Since then the many aspects of adatom-adatom interactions have been studied in greater detail, with papers spanning several decades even up until recently [18] [19] [5] [20] [21] [4].

(a)

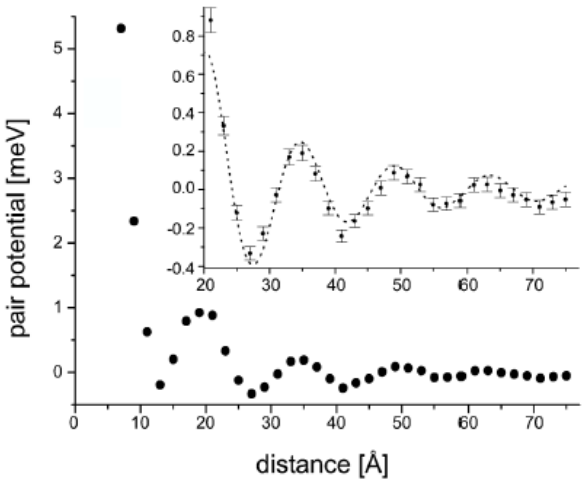

(b)

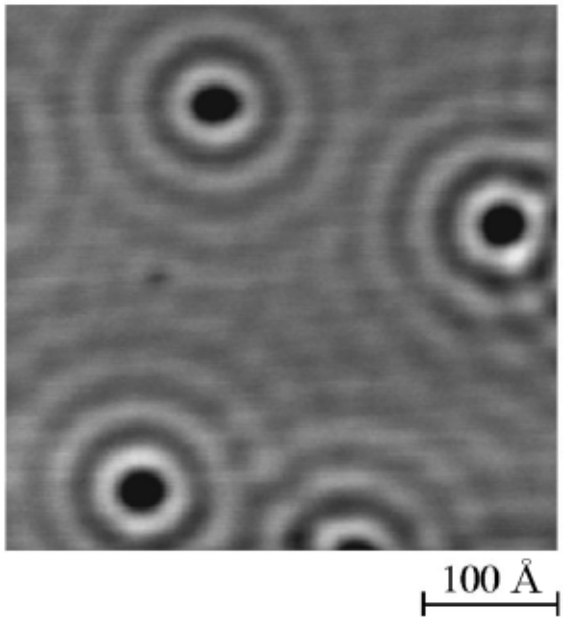

Figure 1.3: a) Adatom-adatom pair potential for Cu on Cu(111), with inset showing magnification of curve at larger separation. Image from [4]. b) STM image, with given scale of 100 Å, showing long range oscillations in the surface LDOS due to the presence of Co defects on Ag(111). Image from [5]

We show an example of these results, namely adatom-adatom pair po-

tential and STM topography, in Fig. 1.3. Among these are quantitative studies of the surface's local density of states (LDOS), enabled by the development of scanning tunnelling microscopy (STM) [22] [23], which allows direct observation of the electron density wave patterns due to the presence of adatoms, as well as the energy spectrum indicative of the density of states (DOS). By fitting these measurements to those produced by theoretical models even more detailed information about the system can be calculated, such as the surface band structure, interaction energies and scattering properties.

Being able to measure, calculate and understand such long range effects is of vital importance, since they can be the dominant factor in processes such as epitaxial growth which is used for semiconductor and nanotechnology fabrication.

1.2.2 Self Assembly of superstructures

Self assembly behaviour can be observed in numerous environments, with some examples at the molecular and quantum level shown in Fig. 1.4. The phenomena we have been discussing, that of long range interactions between adatoms on surfaces, also brings with it the possibility of a self assembly mechanism. We could imagine multiple interaction effects combining, such that the induced surface LDOS wave pattern would keep adsorbed atoms locked in a single position, corresponding to the point of minimum energy, and so creating extended superstructures at the atomic or molecular scale.

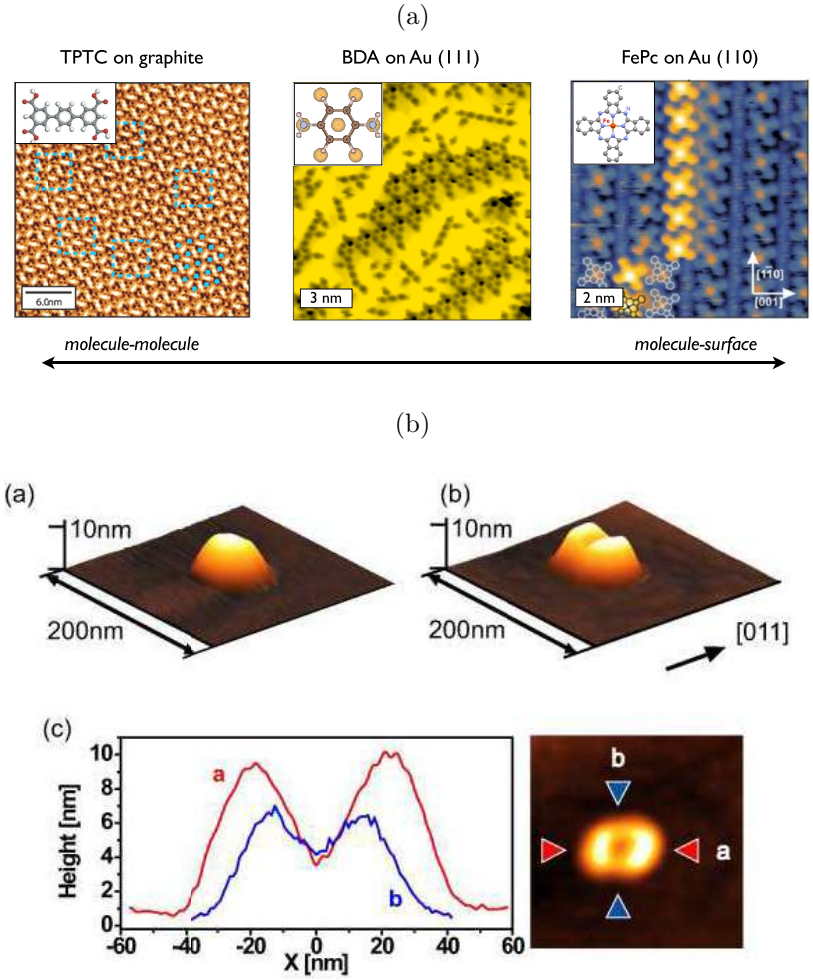

Figure 1.4: Self assembly is a subject of interest across many scientific disciplines, such as for studying its impact on a) molecular deposition on surfaces [6] and b) even its use in the creation of quantum dots [7].

However in practice only relatively few cases of self organised atomic super-lattices have been observed or explained. These include the previously mentioned Ce/Ag(111) system [1] [2] [24], Ce/Cu(111) [25], Gd/Ag(111) [26], and a quasi-super-lattice in the case of Fe/Cu(111) [27] [28] [1].

Our work develops on a particular study of Ce/Ag(111) which used a tight binding model for the substrate surface, and included the impurity through

[1] We specify this instance as a "quasi-lattice" as it did not demonstrate long range order, but rather numerous regions or islands of regular adatom separation

a local ionic potential [2] [23] which modified the crystal field. This found that the creation of a stable super-lattice occurs as a consequence of Friedel oscillations, movements in the substrate's free electron states which drive adatoms to move across the surface, representations of which are shown in Fig. 1.5.

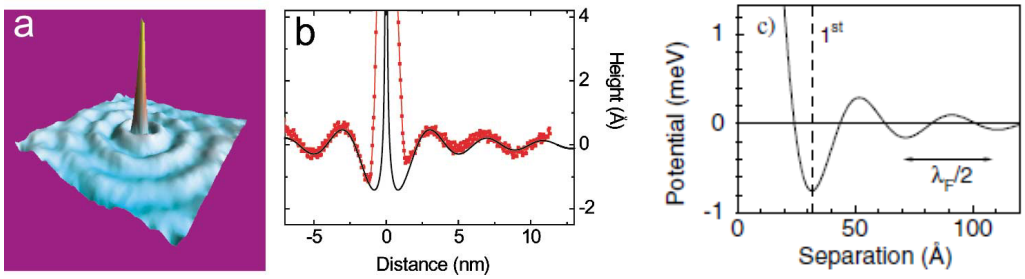

Figure 1.5: Figures showing Friedel oscillation pattern around a Ce adatom and the resulting adatom-adatom interaction potential, with a first minima at the observed separation. Image from Ref. [2].

The adatoms are mobile until they are separated by a distance corresponding with the minima of the adatom-adatom interaction energy, at which point the resulting periodic perturbation to the crystal field from the ionic potentials opens a band gap, suppressing further movement of the surface electrons and adatoms. Fig. 1.6 shows this gap opening in the theoretical surface band dispersion, which corresponds well with the observed gap opened in the Ce/Ag(111) spectra as seen in Fig. 1.7. However this model predicts similar behaviour for any ionic potential, or modification of the crystal field, meaning for any species of adatom.

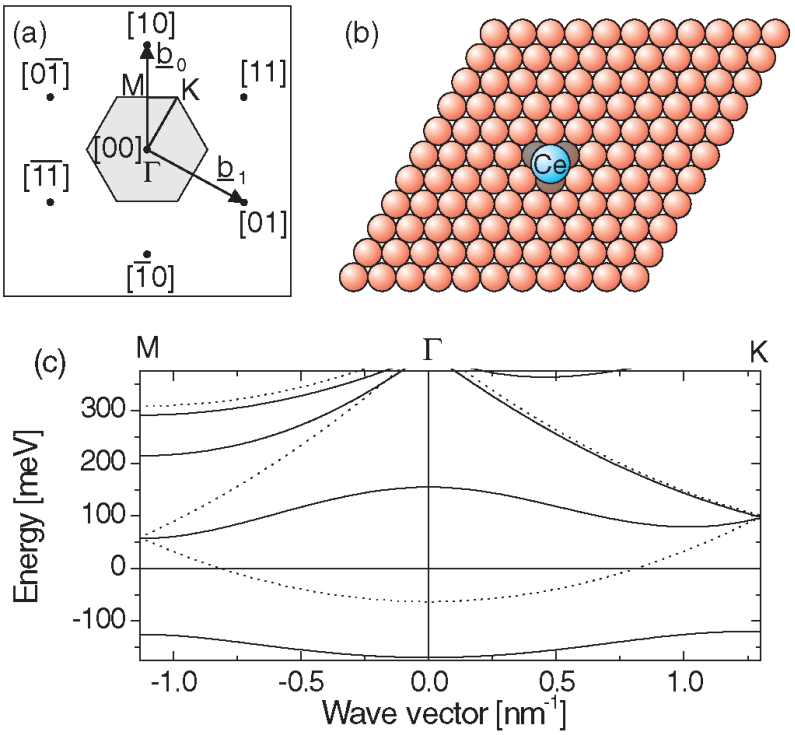

Figure 1.6: a) Diagram of the reciprocal space Brillouin zone with points along the band structure k-point path indicated. b) Schematic of the unit cell used for tight binding calculations with an adatom situated on top of 3 substrate atoms. c) The band dispersion along the indicated k-point path of the surface when clean (dashed line) and including the adatom impurity (solid line), showing a gap opening as a consequence of the ionic potential. Image from Ref. [2].

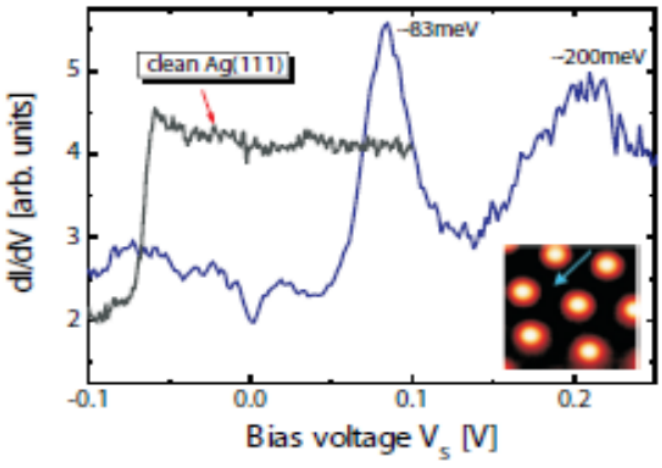

Figure 1.7: Spectra produced using STM spectroscopy measurements of both the clean Ag(111) surface and of the Ce super-lattice with adatom separation of 3.2 nm. Inset is the STM topography image of the super-lattice's hexagonal unit cell. Image comes from the corresponding poster of Ref. [2].

The current standing of research then is that while there have been numerous experimental investigations into transition and rare earth impurity deposition on metallic surfaces [18] [19] [5] [20] [21] [4], and although there is evidence of long range surface-mediated interactions, the majority of these do not result in long range order. For instances where super-lattices have been observed their formation has been well supported by tight binding models and kinetic Monte Carlo simulations [1] [2] [24], Ce/Cu(111) [25], Gd/Ag(111) [26].

However, the current models do not account for the rarity of this phenomena, as their proposed mechanism, which can be encapsulated within a simple tight binding description, makes no significant distinction between adatom and surface elements and suggests super-lattice formation should

be much more wide spread. We note that theses models lack the capacity to capture the more complex effects, which are borne out of strongly correlated behaviour and discussed in the next section, that could significantly contribute to the observed phenomena. We propose that the inclusion of the Hubbard U repulsion on the impurity is vital for understanding and modelling adatom super-lattices, particularly since such strong local interactions are known to be important for f- and d-orbital elements.

1.2.3 Strongly correlated behaviour on surfaces

Strong correlation refers to the presence of strong electrostatic repulsion between electrons as a consequence of highly localised atomic orbitals, a characteristic of the 4f bands of lanthanides and the 3d bands of transition metals. Elements that exhibit this behaviour are sometimes referred to as heavy fermions, based on the increased effective mass of the bound electrons. This local effect can have a significant impact on a larger system, as it directly effects electron movement and occupation, and can give rise to a number of phenomena in the case of adatoms deposited on surfaces.

Among these are: the Kondo effect, a result of electron screening and scattering off a magnetic impurity, as shown in Fig. 1.8; and the RKKY interaction an indirect correlation of impurity magnetisation mediated by conduction electrons, with the distance dependence demonstrated in Fig. 1.9. There are numerous reviews of both: the Kondo effect, with studies into its role in adatom behaviour [8] [29] [30] [31] [32] [33] [34] [35] [36] [37]

[38], in particular how this effects STM measurements; and RKKY [39] [30] [34] [35] [40] [18] [41] [9]. We refer in Fig. 1.8, and throughout this work, to the spectral function rather than density of states, which is defined in terms of single particle energy levels which do not strictly exist in an interacting system [42].

The Kondo effect was suggested in Ref. [1] as a possible reason for why the Ce super-lattice on Ag(111) may remain stable in the absence of Friedel oscillations, and previous work into Kondo scattering from Ce on Ag(111) existed previously to this [43].

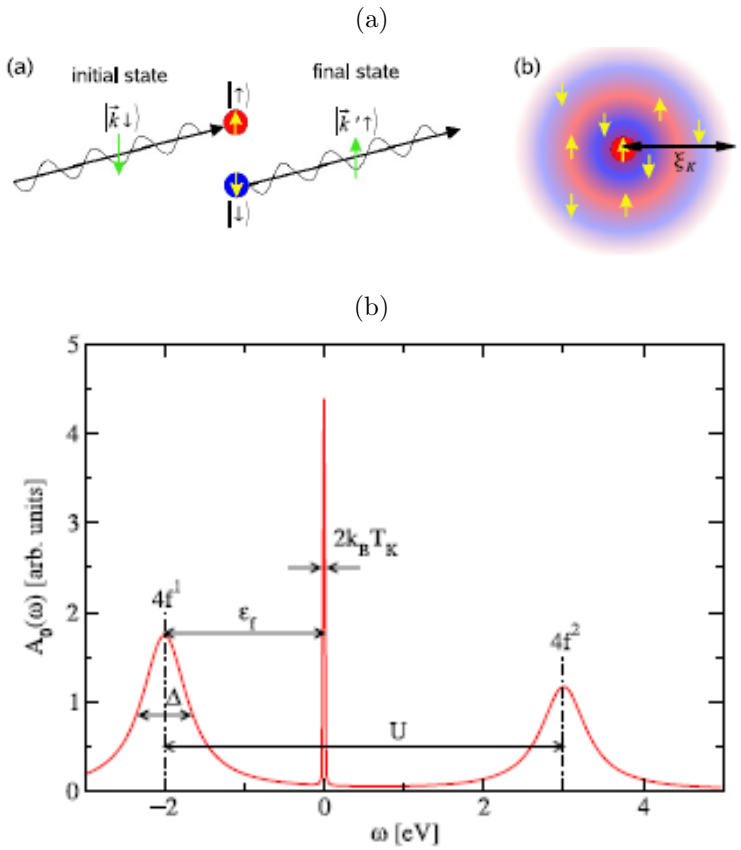

Figure 1.8: a) Diagram of the Kondo scattering process. b) 4f spectral function of a single cerium impurity showing the split Hubbard bands and Kondo resonance at the Fermi level. Images from [8].

(a)

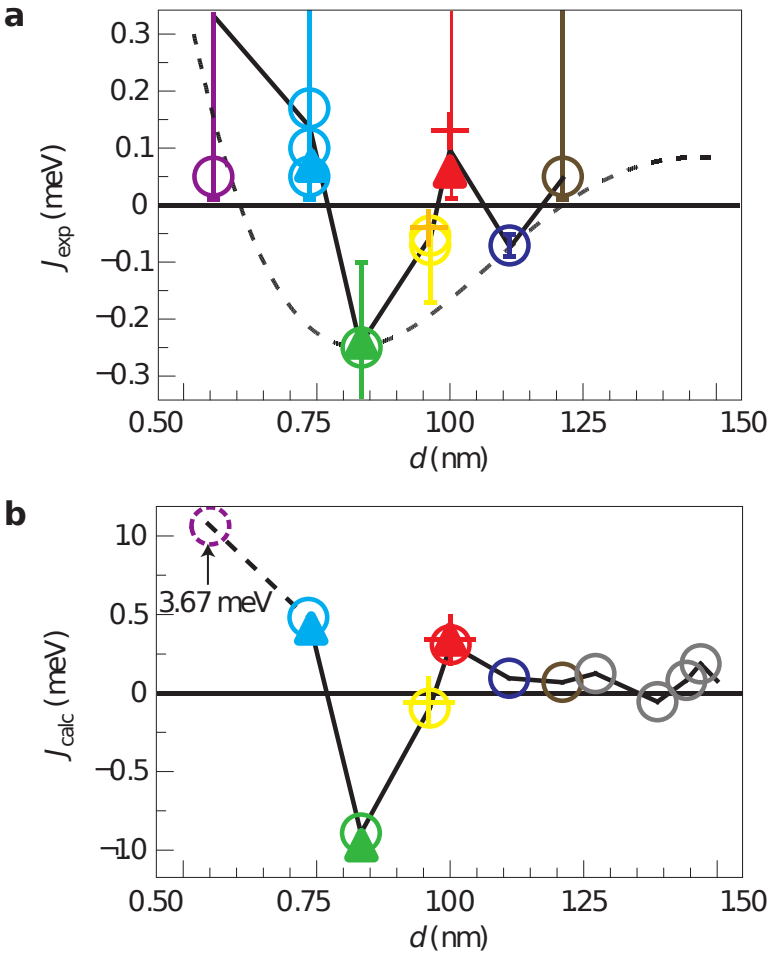

Figure 1.9: Experimental and calculated distance dependence of the RKKY interaction between Co groups on Pt(111). The colours and shapes used correspond to Co pairs or triplets and their relative positions, as indicated in Fig. 2 of [9].

Other examples of heavy fermion systems include Mott insulators [44] [45] [46] and [47] [48] [49]: transition metal compounds predicted to be metals by band theories, but due to the strongly localised nature of their 3d orbitals incur a Hubbard U energy penalty for their double occupation, preventing conduction. Given that the strongly correlated nature of heavy fermion systems is found to be a critical factor in system behaviour for a

multitude of cases, we are confident that its inclusion into the description of super-lattices will have a significant contribution to the phenomena found.

1.3 Aim of this work

While previous work does provide a good description of super-lattice formation in some particular cases, the reason why only a few adatom-surface combinations should form stable super-lattices, when many others elements also present long range surface mediated and adatom-adatom interactions on metal surfaces, is so far elusive. The models used are also relatively simplistic in regards to the interactions included and are unable to capture more complicated effects that might arise from strong electron correlations, which we expect to be a significant factor given the highly localised orbital nature of the lanthanide and transition elements considered.

Our aim is to take a different but complementary approach to this problem, using dynamical mean field theory (DMFT) [50] to properly describe the strong f-orbital correlation of lanthanide metals on top of a tight binding surface lattice, to produce phase diagrams offering a more general overview of super-lattice systems. Our investigation into this more general case of strongly correlated impurities on a triangular (111) surface reveals a rich spectrum of phenomena, arising from the competition of localisation and itinerancy, and the inclusion of Hubbard U adds considerable complexity to the previous tight binding results.

Chapter 2

Thesis overview

In the following chapters we present our work on including the Hubbard U interaction into the study of large scale ordered super-lattices and our analysis of its effects. We have begun in chapter 1 by introducing the problem and setting out our motivations for studying it. In section 1.2 we discussed the previous work relating to this topic and explained how our investigation moves beyond these simple models.

We proceed in chapter 3 to introduce the concept of strong correlation and how this effect is described by several models. We show how our system can be mapped onto the single impurity Anderson model, but how the non-trivial dependence of Hubbard U prevents simple projection onto reciprocal space, which would simplify the modelling of a many impurity real space lattice as a single k-dependent unit cell. We employ dynamical mean field theory (DMFT) [50] in chapter 4 to circumvent this problem, employing an auxiliary impurity solver system to define a self consistency loop which converges a quantity called the self energy, Σ, which contains the purely local, k-independent effect of U. As part of our theoretical treatment we discuss several mathematical techniques used as part of this process.

In chapter 5 we elaborate on the computational methods we have employed to make our code more efficient, reducing the memory and time needed to achieve successfully converged simulations, and share a pseudo-code to illustrate how we implement the DMFT algorithm.

We move on to the presentation and discussion of our results, beginning in chapter 7 with a demonstration that our model gives results consistent with the strong coupling limit in several important ways. We then progress in chapter 8 to what we term the intermediate correlation regime, where we introduce a stronger hybridisation by using the ED impurity solver [51] which promotes itinerant behaviour in competition with the localisation effect of U.

We explore the phase space of adatom super-lattice systems, namely by varying adatom separations and total electron densities. In doing so we demonstrate how such changes effect the properties of impurity occupation, impurity magnetic moment and the Z function, a measure of strong correlation. From these results we endeavour to explain certain trends in system behaviour. Further to this we briefly examine extensions of this method to deal with many impurities (cluster DMFT, or CDMFT [52]) which can allow the study of impurity-impurity interactions such as indirect RKKY [39] exchange, an example of which we include as proof of concept and ability.

We draw preliminary conclusions on what interactions play important roles in the observed formation of a Ce super-lattice on Ag(111), our main observation being that the strong correlation embodied by U serves to isolate

a singly occupied impurity, preventing hybridisation with the surrounding surface bath and leaving the adatom's ionic potential as the only artefact of its presence. It is for this reason that we believe strongly correlated elements such as lanthanides and some transition metals will form large scale ordered super-lattices according to a tight binding description, which only includes their ionic potentials.

Finally we discuss the future work necessary to complete the picture we begin to uncover, such as considering the effect of disorder, performing DFT [53] calculations prior to a DMFT treatments and more expansive cluster DMFT work to capture magnetic behaviour due to RKKY. It is our hope that this work will allow more deliberate probing of complex super-lattices, both experimentally and theoretically, giving important indications of what regions of electron density and temperature interesting phenomena will occur and with what species of adatom they may be found.

Part II

Methodologies

Chapter 3

Theoretical Models

3.1 Describing Strong Correlation

Before introducing the DMFT methodology we will introduce and elaborate on the concept of strong correlation and how it can be modelled. Beginning from the case of non-interacting interactions, we can describe a lattice of sites with nearest neighbour hopping by the tight binding Hamiltonian [54] [55],

$$H_{TB} = -t \sum_{<i,j>} c_i^\dagger c_j + h.c. \tag{3.1}$$

where $c_i^\dagger(c_i)$ are the creation (annihilation) operators for an electron on site i. Hopping with amplitude -t is allowed between nearest neighbours $< i,j >$, with the hermitian conjugate included to allow this process in both directions.

If we then consider what the contribution to this would be from electron-electron interactions, it can be found that the most important terms come from electrons situated on the same site. Adding this to the tight binding

Hamiltonian and including the electron spin explicitly for all terms gives the Hubbard Model [56] [57] [58],

$$H_{HM} = -t \sum_{<i,j>\sigma} (c^{\dagger}_{i\sigma} c_{j\sigma} + h.c.) + U \sum_i n_{i\uparrow} n_{i\downarrow} \tag{3.2}$$

with $n_{i\sigma} = c^{\dagger}_{i\sigma} c_{i\sigma}$. The Hubbard Model describes a lattice of strongly correlated sites, where electrons can hop to nearest neighbours and experience a strong Coulomb repulsion, with energy cost U, when occupying the same site. In the limit of half filling and *U=0* this returns to the tight binding model, giving metallic behaviour, but in the limit $U \to \infty$ the cost of double occupation becomes so large that electron positions are frozen and the system becomes a Mott insulator. Between these limits there is competition between the terms, which encourage itinerant and localized behaviour respectively.

At large U, where it is still most energetically favourable for sites to be singly occupied but hopping between sites can occur in the context of an exchange interaction, the system can instead be described by the t-J model [59] [60] [61] [62],

$$H_{t-j} = -t \sum_{<i,j>\sigma} (\bar{c}^{\dagger}_{i\sigma} \bar{c}_{j\sigma} + h.c.) + J \sum_{<i,j>} (S_i S_j - \frac{1}{4} \bar{n}_i \bar{n}_j) \tag{3.3}$$

where there now exists an exchange coupling J dependent on nearest neighbour occupations and spin. The operators are redefined by $\bar{c}_{i\sigma} = (1 - n_{i\sigma})c_{i\sigma}$.

These models are insufficient for describing our system, which is not a lattice of impurity sites but rather impurities spread dilutely across a surface. However, the Hubbard Model does serve as the basis for a more appropriate model, the Anderson Impurity Model.

3.2 Modelling a super-lattice - The Anderson Impurity Model

The system we study is a very large lattice problem, with many adatoms spread across even more surface atoms. The Hamiltonian for describing this system, shown in Eq. 3.4, is the Anderson Impurity Model or AIM [63] [62] [64]. This is built upon the Hubbard Model by including separate impurity states which can hybridise with the nearest neighbour sites on the surface lattice, which is described as a tight binding conduction band. We also include at this point the impurity ionic potential and explicitly the chemical potential. Impurity simply refers to the strongly correlated adatom which exists within an environment of non-correlated neighbours.

$$\begin{aligned} H_{AIM} = & -t \sum_{<i,j>\sigma} (c^{\dagger}_{i\sigma} c_{j\sigma} + h.c.) + \sum_{i\sigma} \epsilon_{imp} f^{\dagger}_{i\sigma} f_{i\sigma} \\ & + \sum_{<i,j>\sigma} (V_{ij} c^{\dagger}_{i\sigma} f_{j\sigma} + h.c.) \\ & + \sum_{f} U n_{f\uparrow} n_{f\downarrow} + \mu \hat{N}_{tot} + \sum_{i,\sigma} V_i c^{\dagger}_{i\sigma} c_{i\sigma} \end{aligned} \tag{3.4}$$

The terms seen from left to right are defined as such: $-t \sum_{<i,j>\sigma} (c^{\dagger}_{i\sigma} c_{j\sigma} + h.c.)$ is the nearest neighbour hopping of the uncorrelated surface state conduction electrons between sites (i, j) with amplitude t; $\sum_{i\sigma} \epsilon_{imp} f^{\dagger}_{i\sigma} f_{i\sigma}$ is contribution of the impurity energy level ϵ_{imp} for each adatom present; $\sum_{<i,j>\sigma} (V_{ij} c^{\dagger}_{i\sigma} f_{j\sigma} + h.c.)$ is the hybridisation V_{ij} between adatoms and the nearest surface state conduction bands; $\sum_f U n_{f\uparrow} n_{f\downarrow}$ includes the Hubbard U repulsion in the case of a doubly occupied impurity orbital; $\mu \hat{N}_{tot}$ is the chemical potential contribution for the number of occupied levels N_{tot}; and $\sum_{i,\sigma} V_i c^{\dagger}_{i\sigma} c_{i\sigma}$ contains the effect of the impurity ionic potential on the nearest surface state sites, as used in earlier TB studies. The adatom - substrate hopping parameter $V_{if} = V^{*}_{fi} = t_{Ad}$ for the three substrate atoms nearest to the adatom, and zero for all others, and similarly for the adatom ionic potential V_i.

At this point we are faced with the complexity of the problem we wish to solve. Although the Hamiltonian is easy to write down, it involves electron hopping interactions between combinations of surface electrons and impu-

rities, as well as strong correlation on the impurity sites and the presence of the adatom ionic potential. In a realistic system there are also many sites to consider.

Consider the Hamiltonian in a matrix formulation, shown below in Eq. 3.5, where each shown quadrant corresponds to a matrix: H_{ij} describes the tight binding surface states; $\epsilon_i + U n_{i\uparrow} n_{i\downarrow}$ is a diagonal matrix describing the local impurity levels and occupation of i adatoms; and V_{ij} and its Hermitian conjugate describes the interactions between the surface and adatoms.

$$H = \begin{pmatrix} H_{ij} & V_{ij} \\ V_{ji}^{*} & \epsilon_i + U n_{i\uparrow} n_{i\downarrow} \end{pmatrix} \tag{3.5}$$

If we consider the observed Ce/Ag(111) case with an adatom - adatom separation of 3.2 nm (or 11 lattice parameters), then a possible unit cell of the system contains a single impurity and 121 surface atoms. The single impurity Hamiltonian thus has the dimensions 122×122 - already a difficult problem to tackle. The realistic system contains multiple impurities, all with a possibly unique but inter-dependent occupation and hence Hubbard term, meaning all must be considered directly. It is clear that such a task quickly becomes computationally prohibitive.

Seemingly intractable problems like this are not unfamiliar in the field of condensed matter physics, with even non-interacting systems being beyond solving at one time. The development of Density Functional Theory (DFT)

[53] overcame numerous difficulties of solving a many body, interacting wave function, with a key feature of the method being a self consistency loop to converge the density, on which the total energy functional and hence all other derivable quantities depend.

DMFT [50] offers a similar solution, via a simple but powerful approximation which results in the replacement of the Hubbard U term with a k-independent quantity denoted Σ , the self energy. This will enable the use of periodic boundary conditions and allows us to consider instead the k-dependent Hamiltonian shown below in Eq. 3.6.

$$H_k = \begin{pmatrix} H_{ij}^k & V_{ij}^k \\ V_{ji}^{k*} & \epsilon_i + \Sigma \end{pmatrix} \tag{3.6}$$

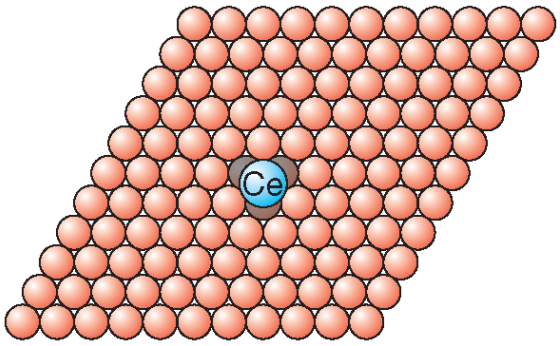

Figure 3.1: Diagram of a possible unit cell for the DMFT calculation, with the Ce sitting in the centre of 3 Ag atoms. Image from Ref. [2].

In order to see how we can arrive at this via DMFT, we start by considering just a single correlated adatom on a truncated surface, such as in the unit cell for the previous tight binding work shown in Fig. 3.1. Such a

system can be described by a particular case of the more general Anderson Impurity Model, the Single Impurity Anderson Model (SIAM) [63] [65].

$$\begin{aligned} H_{SIAM} = & -t \sum_{<i,j>\sigma} (c^{\dagger}_{i\sigma} c_{j\sigma} + h.c.) + \sum_{\sigma} \epsilon_{imp} f^{\dagger}_{\sigma} f_{\sigma} \\ & + \sum_{<i,f>\sigma} (V_{if} c^{\dagger}_{i\sigma} f_{\sigma} + h.c.) \\ & + U n_{f\uparrow} n_{f\downarrow} + \mu \hat{N}_{tot} + \sum_{i,\sigma} V_i c^{\dagger}_{i\sigma} c_{i\sigma} \end{aligned} \tag{3.7}$$

A schematic of the Ce/Ag(111) system with these terms in contexts is shown below in Fig. 3.2. The Ce is shown hybridising with 3 Ag, as we think it most physical that the impurity sit in the centre of the Ag triangular symmetry. The Ce sits at the impurity level energy E_{imp}, and hybridises V_{Ce-Ag} with the Ag atoms which have been reduced in energy V_{Ce} by the cerium's ionic potential. The Ag have hopping t with nearest neighbours.

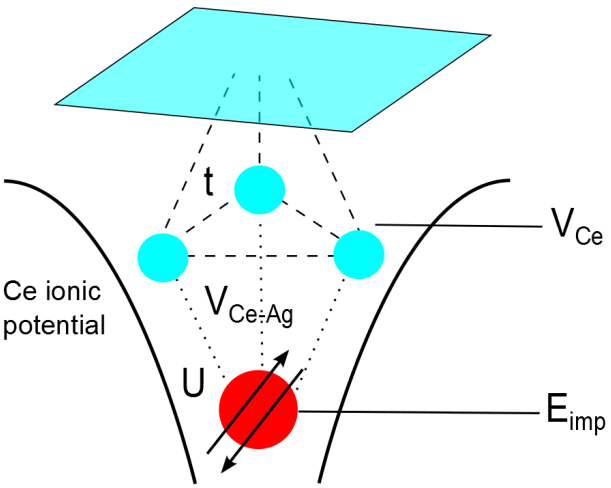

Figure 3.2: A diagram of the system at a single impurity, showing the interactions and energy levels contained in the AIM Hamiltonian for the case of double Ce occupation.

We might now reasonably consider that if our single adatom system can be described in this way, then a much larger system of which it is the unit cell could be described similarly through application of periodic boundaries, which would introduce a sum over k points to each term. This supposition holds true for all terms except one: Hubbard U, which cannot be simply collapsed into a single impurity, k-dependent term.

This becomes clear if we consider what this term represents: the occupation of an impurity site, which can be one of 4 states: empty, singly occupied with an up or down electron, and doubly occupied, which incurs an energy penalty of magnitude U. This state is the result of many body effects, due not only to hybridisation with the immediate surface states but indirectly with the occupation state of all other impurities. In a system with N impurities, each with a possible 4 states that are interdependent with the others, there are 4^N terms to consider, which is prohibitively large. Each site has a different term, and to treat each individually would require us to solve the AIM for each k point with a different, interacting U term - we essentially go back to our original intractable problem. What we really want is to represent all of our impurities by a k-point averaged single impurity Green's function [66], which contains an average effect due to U. Such a quantity does exists and is known as the self energy, and the method by which we obtain it is called dynamical mean field theory.

Chapter 4

Dynamical Mean Field Theory

Here we shall give an introduction to the principles of DMFT using the AIM. It is a still growing field of interest with reviews still being written and updated even now, and we refer the reader these [50] [67] [68].

The power of DMFT comes from considering the limit of infinite dimensions, or coordination number, where impurities are completely surrounded by nearest neighbours. Further discussion of this can be found in [67] and [69], which demonstrate that in the limit of infinite dimensions the self energy becomes local, ie k independent. The consequence of this is that the effect of U is purely local and independent of the impurity considered. This amounts to telling us that the effect of U can be described by a k-independent, averaged quantity known as the self energy, Σ. Although this statement is only exact in the limit of infinite dimensions, even in as small a number of dimensions as 2 and 3 it can be remarkably powerful.

This also means that we should be able to equate the local physics contained in our real system with many impurities to those found in a much simpler k-dependent single impurity case, and indeed the essence of DMFT lies in its mapping of the large scale, intractable lattice problem, onto a sin-

gle site impurity problem. In both cases we not only consider an averaging of the effect of U, but also of the impurities' interactions with the surrounding sites, which we incorporate into a quantity known as the hybridisation, Δ. This is the k-independent mean-field, which along with the dynamical effects captured by itself and the self energy is what gives the theory its name. DMFT encapsulates the process by which we obtain Σ through the use of Green's functions and the application of self consistency conditions, which shall be the subject of the next section.

4.1 The Green's Function Method

Green's functions are DMFT's method of choice for solving the Hamiltonian, and have the added benefit that many physical quantities, such as the density of states, can be defined directly from them, and so make calculation of relevant results quick and easy. We will keep to a brief description based on the methods set out in [62] and [68]. More detailed accounts of the definition of the Green's function, its Matsubara form and its derivations in the case of the Hubbard and non interacting Hamiltonians can be found in [55] [70] [71] [66].

As discussed, a consequence of considering infinite dimensions is that the impurity embedded in the real lattice system, described by G^f_{loc}, can in the limit of infinite dimensions be equated to a single strongly correlated impurity sitting within a mean field bath, described by G_{imp}, as shown in Eq. 4.1.

$$\begin{aligned} G^f_{loc}(i\omega_n) =& \frac{1}{N_k}\sum_k G^f_k(i\omega_n) \\ =& G_{imp}(i\omega_n) \\ =& \frac{1}{i\omega_n + \mu - \epsilon_{imp} - \Sigma_{imp}(i\omega_n) - \Delta_{imp}(i\omega)} \end{aligned} \tag{4.1}$$

with the approximation $\Sigma_{imp} = \Sigma_{latt}$ and $\Delta_{imp} = \Delta_{latt}$.

The Matsubara frequencies are defined as

$$\omega_n = \frac{1}{\beta}(2n+1)\pi \tag{4.2}$$

where β is inverse temperature.

The hybridisation can be seen as the dynamical mean field of our system, containing the contribution of the substrate conduction band dispersion and the hybridisation of this with the impurity. In physical terms it describes the case of an electron leaving the impurity, travelling through the bath, and then returning. The self energy is the contribution of the on site repulsion, but is now a purely local quantity due to being k independent. However, we still do not know the form of this term, and so are still unable to calculate it directly.

This problem is tackled by introducing a simplified impurity solver model that incorporates the Hubbard U explicitly, and from which we can calculate

the impurity Green's function, G_{imp}. The self energy can then be defined as

$$\begin{aligned}\Sigma_{imp}(i\omega_n) &= G^{-1}_{0,imp} - G^{-1}_{imp} \\ &= i\omega_n + \mu - \epsilon_{imp} - \Delta(i\omega_n) - G^{-1}_{imp}\end{aligned} \tag{4.3}$$

where $G^{-1}_{0,imp}$ is the non-interacting Green's function and the hybridisation is defined in this first instance from the non-interacting total lattice system and used according to $\Delta_{imp} = \Delta_{latt}$.

$$\Delta(i\omega_n) = i\omega_n + \mu - \epsilon_{imp} - (G^f_{loc})^{-1} \tag{4.4}$$

Having calculated a self energy, we can use the approximation $\Sigma_{imp} = \Sigma_{latt}$ to insert this into the Hamiltonian of the total lattice system, obtain a new local Green's function from which we can define an updated hybridisation, which can once more be used as an input to the impurity solver. This process defines a self consistency loop, wherein the self energy and hybridisation continually inform each other until the changes fall below a specified precision.

Below in Fig. 4.1 we include a joint schematic - mathematical overview of the DMFT process, with reference to the Ce/Ag(111) system. We then proceed to elaborate on these points in a more general sense.

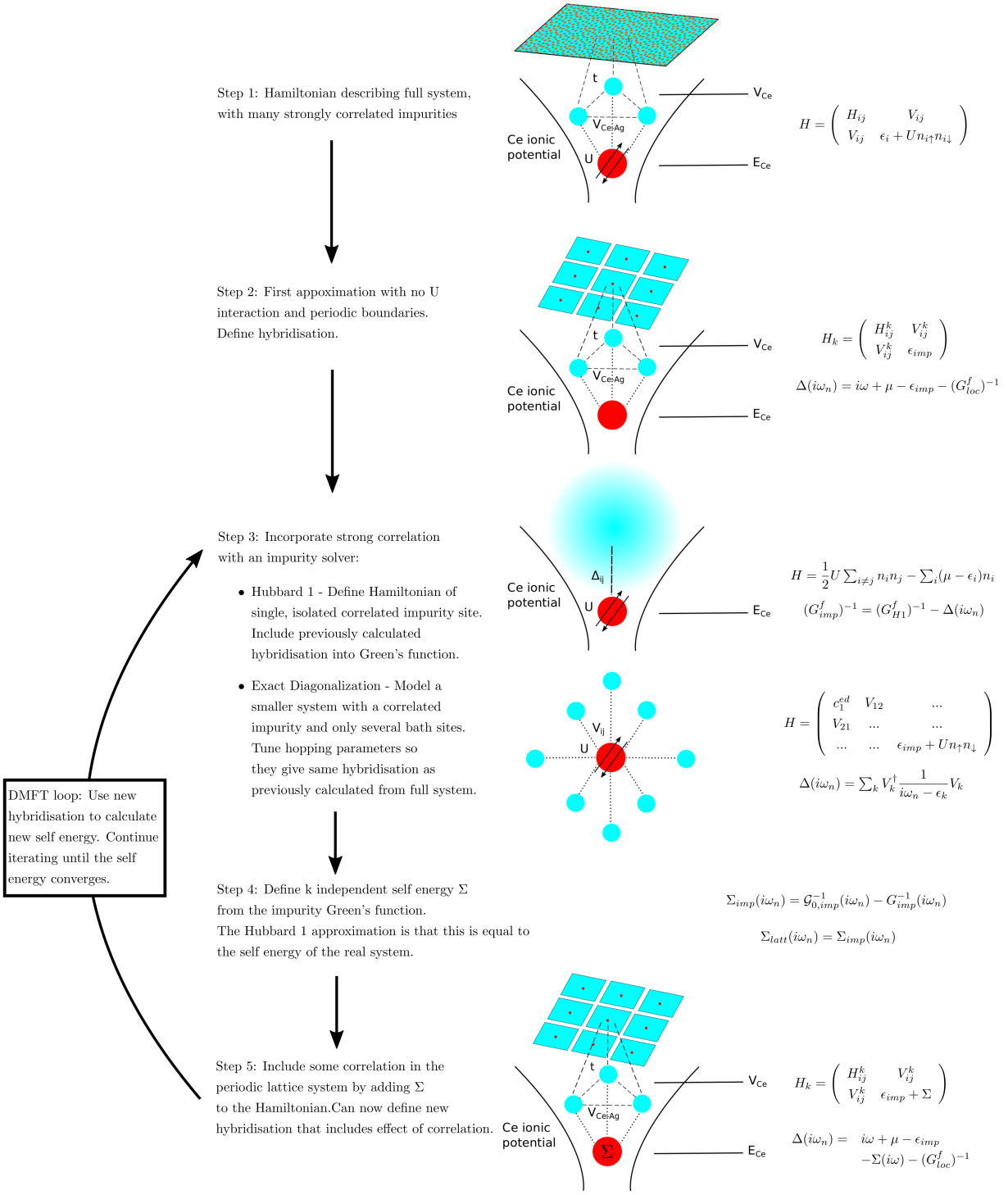

Figure 4.1: Series of schematic and mathematical representations of the physical system and Hamiltonian parameters around a single impurity, demonstrating the DMFT process.

4.1.1 Imposing density via chemical potential

The chemical potential μ is an important quantity for imposing the density of the system and ensuring consistency in density within the impurity solver. We do not employ DFT to obtain an initial Hamiltonian with a converged density, but instead study the effect of varying total lattice and impurity occupation by varying the density. This is encoded in our model through this following expression

$$n = \frac{1}{\beta} \sum_{n=-\infty}^{\infty} G_{loc}(i\omega_n) e^{i\omega_n 0^+} \tag{4.5}$$

We begin by demanding a total density of the system and iterate over chemical potentials until the above expression holds true. With this value of μ we calculate the occupation of the impurity site

$$n_f = \frac{1}{\beta} \sum_{n=-\infty}^{\infty} G^f_{loc}(i\omega_n) e^{i\omega_n 0^+} \tag{4.6}$$

We then require that the impurity solver also return this value for the impurity occupation, which we ensure by further iteration over the impurity chemical potential μ_{imp}.

$$n_{imp} = \frac{1}{\beta} \sum_{n=-\infty}^{\infty} G_{imp}(i\omega_n) e^{i\omega_n 0^+} \tag{4.7}$$

4.2 Impurity Solvers

There are numerous impurity solvers employed, each with limitations and being suited to particular problems. For our investigation we begin with the simplest, the Hubbard 1 Approximation, which ignores the bath hybridisation. We then extend our analysis using exact diagonalisation, a method that reduces the full single impurity Hamiltonian to one with a smaller number of bath sites, making diagonalisation of the matrix feasible. In particular we use the method set out in [72], where cluster perturbation theory (CPT) [51] is also used to include more bath sites, in such a way as to increase accuracy but not significantly alter the computational cost.

4.2.1 Hubbard 1 Approximation

Our introduction to the Hubbard 1 (H1) [73] solver will be informed by [68]. H1 is the simplest impurity solver, which in its purest form neglects the mean field hybridisation, and so considers a purely isolated impurity with a U repulsion. In the general case it describes a multi-band impurity by the Hamiltonian

$$H = \tfrac{1}{2}U \sum_{i \neq j} n_i n_j - \sum_i (\mu - \epsilon_i) n_i \tag{4.8}$$

Here ϵ_i refers to the energy level of impurity band i, and i, j refers to orbital states including the spin σ. From here on we will enforce that all

impurity energy levels are equal, $\epsilon_i = \epsilon \forall i$.

From this Hamiltonian we calculate the energy as a functional of the total number of electrons, N, to be

$$E(N) = \tfrac{1}{2}UN(N-1) + (\epsilon - \mu)N \tag{4.9}$$

Defining the Green's function in imaginary time and performing a Fourier transform results in the imaginary frequency definition

$$G(i\omega_n) = \sum_{N=0}^{L-1} \frac{A_N}{i\omega_n + \mu - \epsilon - UN} \tag{4.10}$$

with coefficients A_N

$$A_N = \tfrac{1}{Z}\binom{L-1}{N}\left[e^{-\beta E(N+1)} + e^{-\beta E(N)}\right], \sum_N A_N = 1 \tag{4.11}$$

where the term Z is the partition function [74] [68].

For our case we only consider a single impurity band which can be at most doubly occupied, so L=2 and this leads to our Hubbard 1 Green's function

$$G_{HI} = \frac{A_0}{i\omega_n + \mu - \epsilon} + \frac{A_1}{i\omega_n + \mu - \epsilon - U} \tag{4.12}$$

The two terms in G_{HI} describe deviations around the impurity ground state, which is when the orbital state is singly occupied. The first term then corresponds to the fluctuation between this and an empty state, and the second with a doubly occupied state, which incurs the U energy penalty.

We can however define a new Green's function, G^f_{imp}, as shown in Eq. 4.13, which combines the effect of U from H1 with the hybridisation as defined from the local Green's function of the original system. This is done in a straight forward manner which we can also use to enforce self consistency, since there will be feedback from the subsequently defined self energy into a new hybridisation. By doing this we include the simplest effects of hybridisation and allow them to be studied with a low computational cost, but our later, more demanding treatment using exact diagonalisation includes this in a more meaningful way.

$$(G^f_{imp})^{-1} = (G^f_{H1})^{-1} - \Delta(i\omega_n) \tag{4.13}$$

The self energy is then defined by comparison to the non-interacting Green's function, shown in Eq. 4.14. The new Σ_{imp} can subsequently be added to the lattice Hamiltonian and a new Green's function and hybridisation defined, which will now contain some elements of local correlation. This process continues to loop until adequate convergence of the self energy has been attained. In our case we instead fixed the number of loops to a value we were confident, after testing, would ensure converged self energies.

$$\Sigma_{imp}(i\omega_n) = \mathcal{G}_0^{-1}(i\omega_n) - G_{imp}^{-1}(i\omega_n) \tag{4.14}$$

4.2.2 Exact Diagonalization and the Lanczos Algorithm

Exact diagonalisation is a method encompassing two parts: firstly, the mapping of our system described by the AIM onto a further auxiliary impurity problem with reduced matrix dimensions; and secondly the tridiagonalisation of this matrix using the Lanczos method, enabling us to obtain the eigenvectors and eigenvalues and calculate the impurity Green's function without a costly matrix inversion. An in depth treatment of both ED and Lanczos is contained in [51], which also contains a thorough discussion of practically implementing the method on modern supercomputers.

The general ED Hamiltonian is show in Eq. 4.15, and through variation of a finite set of parameters V_k, ϵ_k in 4.16, we ensure that the hybridisation of this system is in correspondence with the lattice problem.

$$H^{ed} = \begin{pmatrix} c_1^{ed} & V_{12} & \dots \\ V_{21} & \dots & \dots \\ \dots & \dots & \epsilon_{imp} + U n_\uparrow n_\downarrow \end{pmatrix} \tag{4.15}$$

$$\Delta(i\omega_n) = \sum_k V_k^\dagger \frac{1}{i\omega_n - \epsilon_k} V_k \tag{4.16}$$

The impurity Green's function is defined from the Hamiltonian as

$$G_{ed}(i\omega_n) = \frac{1}{i\omega_n + \mu - H_{ed}} \tag{4.17}$$

This inversion is computationally costly, but can be avoided by calculating the Green's function by the alternate definition

$$G_{ed}(i\omega_n) = \upsilon^\dagger \frac{1}{i\omega_n + \mu - E_{ed}} \upsilon \tag{4.18}$$

where the Hamiltonian has been decomposed into eigenvectors υ and eigenvalues E. These are easily found by the equality below, more commonly known as the time independent Schrödinger Equation,

$$H_{ed}\upsilon = E_{ed}\upsilon \tag{4.19}$$

if H_{ed} is diagonal or tri-diagonal. The latter can be achieved via the Lanczos method, which consists of applying a series of normalised, orthogonal vectors to a Hermitian matrix in the following manner.

Starting with an arbitrary, non zero normalised vector $|\phi_0\rangle$ ($\langle\phi_0|\phi_0\rangle = 1$), we can define a second vector as the following linear combination

$$b_1 |\phi_1\rangle = H |\phi_0\rangle - a_0 |\phi_0\rangle \tag{4.20}$$

and enforcing orthonormality

$$\begin{aligned} b_1 \langle \phi_0 \mid \phi_1 \rangle &= \langle \phi_0 \mid H \mid \phi_0 \rangle - a_0 \langle \phi_0 \mid \phi_0 \rangle = 0 \\ \implies a_0 &= \langle \phi_0 \mid H \mid \phi_0 \rangle \end{aligned} \tag{4.21}$$

$$\begin{aligned} b_1 \langle \phi_1 \mid \phi_1 \rangle &= \langle \phi_1 \mid H \mid \phi_0 \rangle - a_0 \langle \phi_1 \mid \phi_0 \rangle = b_1 \\ \implies b_1 &= \langle \phi_1 \mid H \mid \phi_0 \rangle \end{aligned} \tag{4.22}$$

we see that a_0, b_1 are defined as matrix elements of H in basis set containing $|\phi_0\rangle, |\phi_1\rangle$. We can further define a third vector $|\phi_2\rangle$ in a similar manner

$$b_2 |\phi_2\rangle = H |\phi_1\rangle - a_1 |\phi_1\rangle - c_0 |\phi_0\rangle \tag{4.23}$$

which is orthonormal to both $|\phi_0\rangle, |\phi_1\rangle$, such that

$$b_2 \langle \phi_0 \mid \phi_2 \rangle = 0 \implies \langle \phi_0 \mid H \mid \phi_1 \rangle - c_0 = 0 \implies c_0 = b_1 \tag{4.24}$$

$$b_2 \langle \phi_1 \mid \phi_2 \rangle = 0 \implies \langle \phi_1 \mid H \mid \phi_1 \rangle - a_1 = 0 \implies a_1 = \langle \phi_1 \mid H \mid \phi_1 \rangle \tag{4.25}$$

$$b_2 \langle \phi_2 | \phi_2 \rangle = \langle \phi_2 \mid H \mid \phi_1 \rangle \implies b_2 = \langle \phi_2 \mid H \mid \phi_1 \rangle \tag{4.26}$$

We can now see the trend of defining matrix elements $a_n = \langle \phi_n \mid H \mid \phi_n \rangle$ corresponding to the energy expectation value of a state $|\phi_n\rangle$, and $b_n = \langle \phi_n \mid H \mid \phi_{n-1} \rangle = \langle \phi_{n-1} \mid H \mid \phi_n \rangle$ corresponding to the overlap of adjacent states. In general then we can define a vector $|\phi_n\rangle$:

$$b_n |\phi_n\rangle = H |\phi_{n-1}\rangle - a_{n-1} |\phi_{n-1}\rangle - b_{n-1} |\phi_{n-2}\rangle \tag{4.27}$$

and it can be shown that if $|\phi_n\rangle$ is orthonormal to $|\phi_{n-1}\rangle, |\phi_{n-2}\rangle$ it is automatically orthonormal to all states $|\phi_j\rangle$ where $j < n-2$, as well as non-adjacent state overlaps $\langle \phi_n \mid H \mid \phi_m \rangle = \langle \phi_m \mid H \mid \phi_n \rangle = 0$ where $|n-m| > 1$. The matrix elements of H in the orthonormal basis set $\{|\phi_n\rangle\}$, known collectively as a Krylov space, thus occupy a tri-diagonal matrix.

$$H^{\phi_n} = \begin{pmatrix} a_0 & b_1 & 0 & 0 & ... \\ b_1 & a_1 & b_2 0 & ... & ... \\ 0 & b_2 & a_2 & b_3 & ... \\ 0 & 0 & b_3 & a_3 & ... \\ ... & ... & ... & ... & ... \end{pmatrix} \tag{4.28}$$

This can be completely diagonalised via conventional means using existing libraries such as LAPACK to give eigenvalues and eigenvectors. We can then define a Hilbert space ground-state vector and eigenvalue from those in the Krylov space, with the more eigenvectors and eigenvalues calculated meaning better convergence to the actual value at the cost of computational time.

Once the eigenvectors and eigenvalues are known in the Hilbert space basis, we can finally define the Green's function and complete a single loop of the impurity solver. An advantage of the Lanczos method is actually that the eigenstates it produces can be used to calculate a whole host of functions [51], for example the Green's function can be defined on both the real axis, using the Lehmann representation, as well the imaginary [75].

$$\begin{aligned} G(\omega_n + i0^+) =& \frac{1}{Z} \sum_{n,m} \frac{\left|\langle \phi_n \mid f^\dagger \mid \phi_m \rangle\right|^2}{\omega_n + i0^+ - E_n + E_m} \\ & \times (e^{-E_m \beta} + e^{-E_n \beta}) \end{aligned} \tag{4.29}$$

where the term Z is the partition function [74] [68].

4.3 Double Counting Correction

A long-standing problem with DFT+U/DMFT has the been the necessity of a so-called double counting correction [68] [76], required to remove the inaccurate Hartree contribution to local Coulomb repulsion in DFT that is better taken into account in the additional methodologies.

While we do not use DFT prior to our DMFT calculations we still encounter a double counting problem, arising through our inclusion of an impurity level whose value implicitly contains a Hartree contribution. To see this we can consider the case that the impurity level is a calculated quantity from a DFT energy-minimisation simulation. This energy level, as with all others, will depend upon the ground state properties of the system and its value will be a result of exchange and correlation effects. In our case while we do not calculate the impurity level, instead imposing a value, we must still accept that by definition it is a result of interactions and cannot truly be decoupled from them.

For this reason once we calculate the self energy, which contains all the information about correlation, we must apply a correction to ensure that we do not include this Hartree contribution twice. Were we to not correct this we would introduce a shift to the system energy levels, which amounts to a re-normalization and is not necessarily undesirable. However this change would effect the system, and since we want to ensure we only observe effects due to the additional on-site correlation due to U, we include this double counting correction.

The correction we use is to subtract the infinite frequency limit of the self energy, $\Sigma(i\omega \to \infty)$, which converges to the paramagnetic Hartree-Fock value [68].

4.4 Analytic Continuation

Since we want to model our system at finite temperature the Green's function is initially defined in terms of imaginary time, which due to its periodicity can then be Fourier transformed into Matsubara frequencies, which are defined in terms of the inverse-temperature β [77]. We would however prefer to obtain the final results on real axes, so that they can be better compared to observable quantities. Analytic continuation [78] [79] is the means by which we can project our Matsubara Green's function onto the real frequency axis, its implementation beginning with the substitution $i\omega \rightarrow \omega + i0^{+}$. This is needed only when using the Hubbard 1 solver and not for exact diagonalisation, due to the Green's function in this case being defined from the ground state as determined from the Lanczos algorithm, which can be done in either real or imaginary frequency.

4.5 Band Unfolding

Band unfolding [80] is the process by which we can obtain the band structure of our system's primitive cell, when our simulation and subsequent calculations are done for a supercell. While we employ the supercell approach to properly take into account multiple impurities and minimize boundary effects, when this is projected into reciprocal space via Fourier transform it gives a correspondingly smaller region than the Brillouin zone, which is associated with the primitive cell. Consequently, the band structure of the

system will be contained in this smaller space and, in order to be familiar and properly compared to primitive cell measurements, it must be unfolded into the larger Brillouin zone. The spectral weight of the unfolded Brillouin zone can be obtained from that of the supercell by

$$A(\mathbf{k},\omega)^{\alpha} = \sum_{i,j=1}^{N_{cell}} e^{i\mathbf{k}(\mathbf{R_i}-\mathbf{R_j})}(A^{\alpha}(\mathbf{K},\omega))^{ij} \tag{4.30}$$

where the folded Brilloiun zone containing reciprocal points $\mathbf{K}$ is defined from the real space supercell created from a number N_{cell} of repeated unit cells, each denoted by indices i, j.

Chapter 5

Computational Methods

Once we have reduced the degrees of freedom in our theoretical model enough to make calculations feasible, we can then employ mathematical and computational techniques to make them more efficient. In our description of ED and the Lanczos algorithm we made use of decomposing the Hamiltonian into eigenvectors and eigenvalues, so as to define the Green's function in terms of these and avoid matrix inversion. This is a useful procedure to also apply to our treatment of the lattice Green's function, not only avoiding matrix inversion but also allowing us to store the sparse non-interacting Green's function as much smaller unitary matrices and so save on memory requirements.

We then make use of the Sherman - Morrison identity which means the non-interacting Green's function is all we ever need to store in the memory and we no longer have to invert any more matrices. Instead we treat the self energy as a perturbation to the non interacting Hamiltonian, and decomposing it into row and column vectors we can define a new interacting Green's function.

Optimization of the way we store and calculate the Green's function is

of vital importance in our code, since it is regularly used for calculations of various results, and to both store each Green's function in its entirety or calculate each from scratch whenever needed would be prohibitive.

5.1 Unitary Decomposition

Unitary decomposition begins from the eigenvalue identity

$$Aq = \lambda q \tag{5.1}$$

where q is an eigenvector of the matrix A with eigenvalue λ. We can generalise to include all eigenvectors q which make up the columns of matrix Q, and all eigenvalues which form the diagonal of matrix Λ.

$$AQ = Q\Lambda \tag{5.2}$$

If A is Hermitian, such as a Hamiltonian, then its eigenvectors form a unitary basis set ($Q^{-1} = Q^{\dagger}$) and it follows that

$$A = Q\Lambda Q^{-1} = Q\Lambda Q^{\dagger} \tag{5.3}$$

Then a matrix G defined as

$$G = \frac{1}{z - A} = \frac{1}{z - Q\Lambda Q^{\dagger}} \tag{5.4}$$

can also be written as

$$G = Q^{\dagger} \frac{1}{z - \Lambda} Q \tag{5.5}$$

seen by multiplying by $Q^{\dagger}$ on the left and Q on the right hand sides.

This process therefore avoids matrix inversion at several steps and allows storage of a large matrix G as much smaller unitary matrices and a vector containing the eigenvalues that fill the diagonal of Λ. In our case, we employ this method to store the non-interacting Green's function at each k-point, since this can be easily diagonalised for the eigenvalues and eigenvectors. The matrix A is the Hamiltonian H_k, which has matrices of energy eigenvalues (E_k) and eigenvectors (υ_k). Replacing the z matrix with Matsubara frequencies we get that

$$G_0^k = \upsilon_k^{\dagger} \frac{1}{i\omega_n - E_k} \upsilon_k \tag{5.6}$$

The power of this is that by just storing the relatively small eigenvector and eigenvalue matrices for all k points we can now easily calculate any (k, $i\omega_n$) matrix element of the non-interacting Green's function, which would be a much larger matrix in its entirety. On its own this does not seem so impressive since this doesn't help with storing of interacting Green's functions, which are required past the first DMFT loop. But together with an identity known as the Sherman Morrison Woodbury formula [81] [82] the

storing of G_0 is actually sufficient.

5.2 Sherman-Morrison-Woodbury Formula

The Sherman-Morrison matrix identity [81] [82] relates the inverse of two matrices, when one is the result of small changes in other. This speeds up the calculation of the interacting Green's function by letting us simply include the changes due only to altered self energy elements, without inverting a whole new Hamiltonian or defining new unitary matrices each time.

The formula is as follows for an known invertible matrix A of dimensions $n \times n$, and matrices U,V with dimensions $n \times m$ and $m \times n$ respectively.

$$[A + UV]^{-1} = A^{-1} - A^{-1}U(I + V^T A^{-1}U)^{-1}V^T A^{-1} \tag{5.7}$$

In the special case where U,V are respectively a column and row vector u, v this becomes

$$[A + uv]^{-1} = A^{-1} - \frac{A^{-1}uv^T A^{-1}}{(I + v^T A^{-1}u)} \tag{5.8}$$

This formula is so useful because it replaces an inversion of an $n \times n$ matrix with a potentially smaller $m \times m$ matrix, $I + V^T A^{-1}U$. The dimension m required depends on how many matrix elements of A are perturbed by UV.

We can make use of this latter expression since the change in our Green's

function matrix, the self energy, is only in a single matrix element and can be decomposed into row vectors. If cluster DMFT was used then U,V would have to be matrices and the top formula would be used.

So if our initial matrix A is in fact the non-interacting Green's function G_0, and is perturbed by the self energy matrix which can be decomposed such that $\Sigma = uv$, to define an interacting Green's function G, then we can see that

$$\begin{aligned} G &= [G_0^{-1} + \Sigma]^{-1} \\ &= [G_0^{-1} + uv]^{-1} \\ &= G_0 - \frac{G_0 u v^T G_0}{(I + v^T G_0 u)} \end{aligned} \tag{5.9}$$

This finally shows then that the non-interacting Green's function is all we ever have to store as unitary matrices, since it can be used the self energy to calculate the interacting Green's function at any k-point and ω, whenever it is needed.

Hence by using the combined computational methods of unitary decomposition and the Sherman - Morrison - Woodbury formula we need only ever perform matrix inversion once on the non-interacting lattice Hamiltonian for each k-point, and store only the resultant eigenvalues and eigenvectors, in order to calculate all subsequent interacting Green's functions once the self energy has been obtained. This is a vastly optimized algorithm in terms of computational time and memory resource requirements compared to ma-

trix inversion of interacting Hamiltonians after each DMFT loop and the storing of each Green's function matrix for use in later calculations.

5.3 Implementation of the DMFT algorithm

A significant portion of project time was taken to write and test a program to simulate our system of interest and gather results. Here we present the general algorithm of our simulation as pseudo-code and discuss some aspects of development such as checking run convergence and the implementation of parallel computation.

Algorithm 1 General Simulation Pseudo-code

Initialize variables $\leftarrow$ *Read from param.txt*
Read system parameters: # of ω, k*, system tiling, reciprocal tiling...*
Allocate and define system arrays: site positions, nearest neighbours, reciprocal vectors...
Desired density $= n$
for all U **do**
  $\Sigma_{imp} = 0$
  for # DMFT iterations **do**
    $\Sigma = \Sigma_{imp}$
Require: $\mu \Rightarrow G_{loc} \Rightarrow n$
    for # μ iterations **do**
      while $n[\mu_{imp}] - n_{imp} > required\,precision$ **do**
        Iterate over μ_{imp}
      end while
    end for
    $G_{loc}[\mu] \Rightarrow \Delta, n_f$
Require: μ_{imp}, $\Delta \Rightarrow G_{imp} \Rightarrow n_{imp} = n_f$
    if Using H1 = = .true. **then**
      for # μ iterations **do**
        while $n[\mu_{imp}] - n_{imp} > \delta$ **do**
          Iterate over μ_{imp}
        end while
      end for
    else if Using ED == .true. **then**
      for # μ iterations **do**
Require: $\Delta_{ED} = \Delta$
        while $n[\mu_{imp}] - n_{imp} > \delta$ **do**
          Iterate over μ_{imp}
        end while
      end for
    elseUsing H1 .or. Using ED == .true.
    end if
    $G_{imp}[\mu_{imp}] \Rightarrow \Sigma_{imp}$
  end for
  Perform band unfolding
  Plot results for U: spectral function, band structure, Fermi surface ...
end for

5.3.1 Parallel Computation

We make use of both OpenMP and MPI to utilise the benefits of parallel computing, to make our simulations more time and memory efficient. They are particularly effective in our algorithm due to the regular needs to calculate quantities, such as the Green's function, at numerous k-points, frequencies and atomic sites. The code structure we employ is to parallelize the calculation of quantities at k-points using MPI, with each of these separate processes using OpenMP to parallelize the definition and sum of quantities at frequencies and atomic sites for a given k-point.

5.3.2 DMFT convergence considerations

After a DMFT run has completed, prior to extracting the desired plots and result quantities, it is subjected to a convergence test in which we compare the final two total densities calculated from the Green's function. A more obvious option would be to compare a point on the self energy curve, such as $\Sigma(i\omega_n = 0)$, on the last two iterations. However doing this does not ensure that all other points are similarly converged, a fact which can only be easily surmised by considering the plots visually which is not a quick or easily automated task. Hence we choose instead to require that the total density is converged, as this necessitates the convergence of the Green's function and self energy.

Another challenge, due to the nature of DMFT, in that the self energy is

an approximation and must be converged self consistently. There are many possible obstacles to this in such a complicated system, since we must limit the number of DMFT loops to keep the computational time requirements feasible, but must ensure enough for convergence. In the ED solver we have similar trade off with the number of bath sites included in the Hamiltonian, where we require enough to be accurate without it becoming costly.

In our calculations the number of bath sites varied between 9 and 12, with the larger value used in cases where strongly correlated effects could be particularly important such as in the Kondo regime. It is worth repeating, however, that these things are not known ab initio and there is no universal benchmark for the quantity of DMFT loops, ED bath sites or various other convergence criteria that are needed for accurate calculations. We have found that these requirements can change considerably depending on the system parameters, such as electron density, used.

Part III

Results and Discussion

Chapter 6

Conventions

6.1 Hamiltonian Parameters

Before attempting to model the super-lattice systems using the AIM, we must address the fact that we do not know the Hamiltonian parameters. As our method is not fully ab initio we do not start with calculated values of the Hamiltonian parameters from DFT, nor do we employ experimentally verified numbers, which are hard to obtain. Rather due to the exploratory nature of our study, many of the Hamiltonian parameters are open for choice.

While part of the purpose of our study is to investigate the effect of some parameter's variations, others must simply be given a fixed value. We chose to give fixed values to the impurity parameters, V_{Ad}, E_{Ad} and t_{Ad}, which together determine the species of adatom modelled. We do not claim that the values used correspond to a real element, let alone cerium, and we chose not to vary these as part of our study precisely because there are so many combinations, most of which would be non-physical. Instead it is our view that investigating the effects of adatom species is best left for an ab

initio DFT+DMFT approach, where physically appropriate values for these parameters can be derived.

For continuity we will use the same Hamiltonian parameters for H1 and ED, unless otherwise specified, with the exception of the inverse temperature β. This is because with ED we want to enforce low temperature to study regimes of Kondo, RKKY and Mott. With H1 we study only the simple effect of hybridisation and ionic potential. While we could do this also at low temperature, having a low β broadens the spectral functions, and simply makes features easier to see and discuss. H1 with a high β has been tested, but no significant qualitative difference was seen, with the main effect being to simply shift the chemical potential.

The tight binding hopping parameter, t, is normalised to $t = 1$ and so forms the unit basis for all other specified values, which can then be interpreted as multiples of this. The ionic potential, $V_{Ad} = -3$, has been kept the same as the previous tight binding study. This was chosen in that case to replicate the experimental results, and we too decided to choose our parameters to give an approximation of these.

Left then are the impurity level and hybridisation factors, E_{Ad} and t_{Ad}. When included the hybridisation was set at $t_{Ad} = -2$ and the choice of impurity level is a subject of the next chapter.

6.2 System tiling convention

As a major part of our investigation we vary the adatom-adatom separation to study its effects and by our convention we refer to this by the surface unit cell tiling used. For example the smallest separation considered is when adatoms sit adjacent to each other. Taking into account that they are modelled as sitting in a vacancy between 3 atoms on the triangular surface and that their ionic potential is experienced by these 3 nearest neighbours, we exclude the possibility that there is an overlap of this potential which leads to the single adatom cell and repeated tiling shown below in Fig. 6.1.

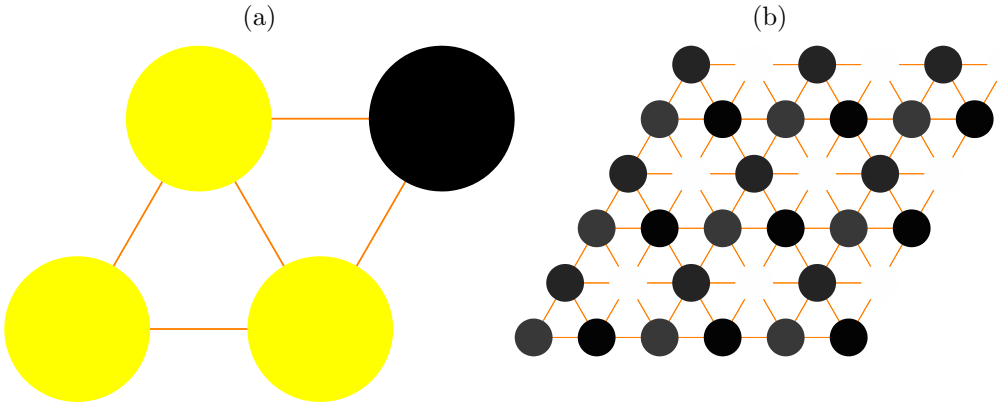

Figure 6.1: a) A 2x2 surface unit cell with the adatom position indicated between the lower left 3 surface atoms as indicated by yellow. b) A tiling of 9 unit cells with adatom positions indicated by black.

This corresponds to a 2x2 tiling, and for results in relation to the total electron density we performed calculations on square tilings in the range 2x2 - 12x12. These were the first results collected, but in our later work, which studied the effect of the impurity occupation, we also included a larger 22x22 tiling shown in Fig. 6.2. On 2D colour plots against the impurity

occupation this tiling has been artificially added to the x-axis by including it as a 13x13 tiling, but does in fact show the extreme limit.

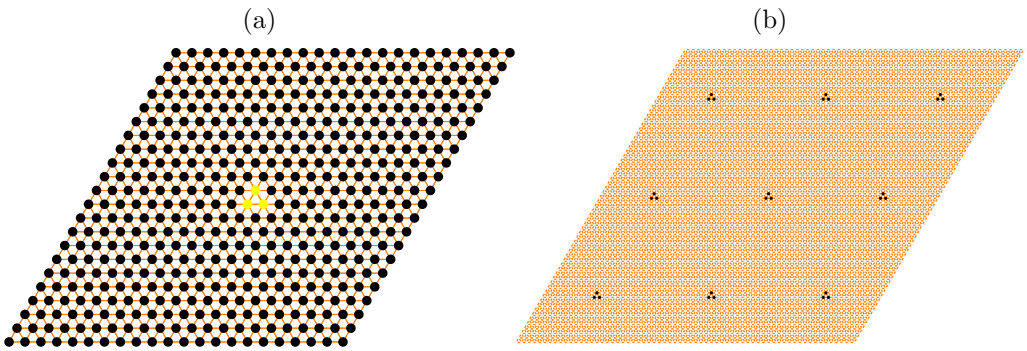

Figure 6.2: a) A 22x22 surface unit cell with the adatom position indicated between 3 surface atoms in the centre as indicated by yellow. b) A tiling of 9 unit cells with adatom positions indicated by black.

6.3 Total density and impurity occupation conventions

The other main variable of our investigation is the electronic density and we vary focus between the total electronic density, n, and the impurity occupation, n_{imp}. The total density is given as a number between 0 and 1, which corresponds to a fractional filling of the total number of electronic states in the system and hence the actual electron number depends on tiling. Hence in the smallest tiling case of 2x2 there are 4 surface atoms and a single impurity, and since each can be doubly occupied at most this means 10 total electronic states. A total density of 0.1 for example would therefore mean a single electron exists in this system. In practice, for results pertaining to the total electron density, namely 2D colour plots, we performed calculations in

the low density regime with n=0.01 - 0.14.

The impurity occupation is also given between 0 and 1, but is the fractional occupation of just the adatom and hence at its maximum value always corresponds to 2 electrons. We performed calculations for the full breadth of impurity occupations n=0-1.

Chapter 7

Strong Coupling Limit

We will begin the presentation and discussion of the results by demonstrating how our model captures the physics of an impurity on a surface in the atomic and strongly interacting limit. In particular we consider how the Hubbard U and adatom separation effect the hybridisation. We use these simple studies to help inform our choice of Hamiltonian parameters, checking it gives results consistent with experiment and the previous tight binding result as a high U limit, although we are more concerned with qualitative rather than quantitative agreement. Once confident in our model and parameters, we implement the running of our code for a range of adatom-adatom separations, total system electron densities and Hubbard U for both the H1 and ED impurity solvers.

While this problem has a whole host of phenomena we could investigate, we have chosen to focus primarily on the role of electron densities, the adatom - adatom separation and the Hubbard U parameter in determining system behaviour. By varying these we are able to map out a portion of the system's phase diagram in detail, and have also gone to the extreme limits of these cases.

However it is noted here, and again in our conclusions, that there is much more to be studied, and what we present is in no way an exhaustive account of the phenomena that could be possible. And indeed it should be reiterated that the exploratory nature of this study, lacking any ab initio or experimentally determined parameters, sets these results apart from the observed case that is our motivation. Although it shall be seen that there are links, as our conclusions will set out, this should be joined with density functional theory (DFT) to allow true ab initio results [79].

7.1 Atomic Limit

We begin by considering the simplest case of a strongly correlated impurity that is isolated entirely from the surface, that is with $V_{Ad} = 0$ and $t_{Ad} = 0$. We set $E_{Ad} = -6$ for this calculation. Our tight binding hopping parameter is always set to $t = 1$ and is the basis for our units, with all other values implicitly expressed in terms of its value. By ignoring hybridisation we can show just the effect of U on the isolated impurity levels. In Fig. 7.1 we show the spectral function [42] of the impurity with U=0 and U=10, with the surface spectral function also shown, for a 2x2 tiling with a total density of 0.1, which means one tenth filled with a single electron.

At U=0 there is a single impurity band situated at the chemical potential but with U=10 it splits into the lower and upper Hubbard bands, indicating single and double occupation respectively. In the absence of any other factors it can be seen that the difference in energy between these bands is

approximately the value of U, since this is the energy cost required to doubly occupy the impurity. This effect of band splitting due to U is characteristic of Mott insulators, but the presence here of the surface state levels between the Hubbard bands makes this more accurately a charge transfer system.

(a)

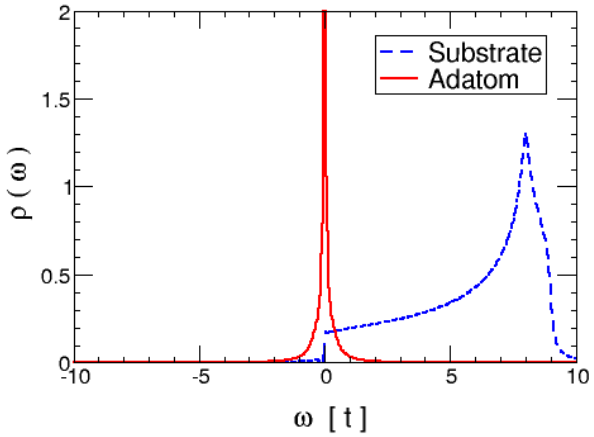

(b)

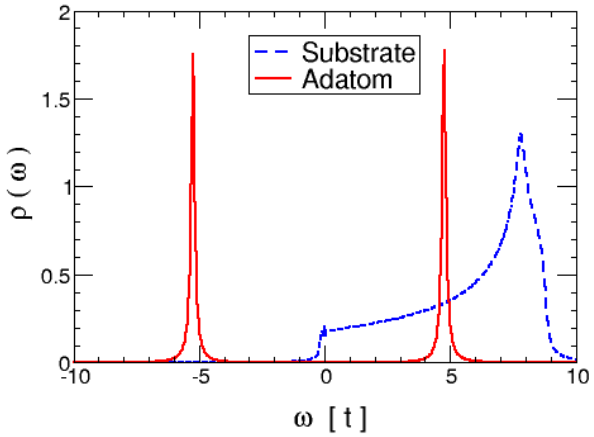

Figure 7.1: Spectral functions of the surface and impurity at the lowest adatom separation and low density, for a) U=0 and b) U=10. It can be seen that a non-zero U splits the impurity band over the Fermi level as in a Mott insulator, but the conduction band exists between them as characteristic in charge transfer insulators.

7.2 Effect of Coulomb Repulsion U

We now introduce hybridisation between the adatom and surface states, and consider how this is affected by the adatom separation and the U repulsion. We do so by varying these individually and present the resulting spectral functions, band structure and Fermi surfaces that demonstrate the impact on hybridisation.

These calculations use the Hubbard 1 impurity solver and for ease our calculations use an inverse temperature $\beta = 1/k_bT = 2$. This high energy serves to make the spectral functions more broadened and the effects of Hubbard bands easier to distinguish, while not missing any of the key features attainable through H1. Additionally all H1 results shown in this section use density n = 0.3, β=2 and $t = 1$, with no V_{Ad} included, $E_{Ad} = -2$ and $t_{Ad} = -2$, unless otherwise stated. The Hamiltonian parameters used for these calculations were picked solely for the clarity of these figures, and as such these results are only for demonstrating the phenomena indicated, and not related to the later studies. The hopping parameter $t = 1$ is the unit basis for all other values.

Firstly, Fig. 7.2 reiterates the atomic limit results but for the new Hamiltonian parameters. The visible horizontal lines indicate the decoupled impurity level, which lies near the middle of the surface band at U=0 and splits symmetrically around that point as U is increased. The x-axis used here, which will be repeated in all band structure results, displays the Brillouin

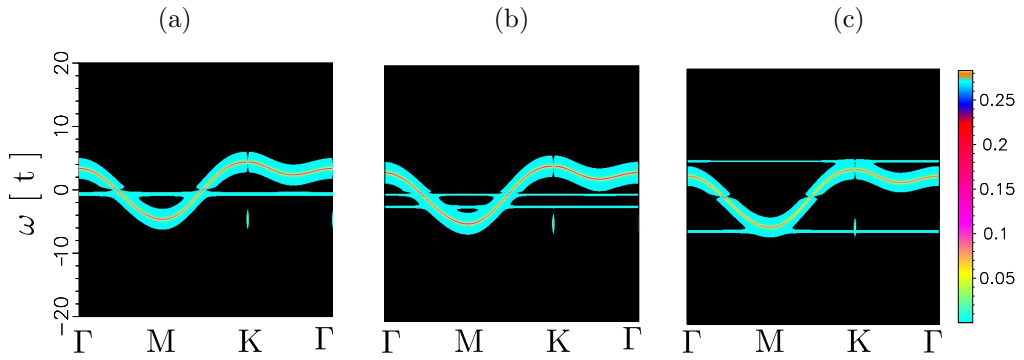

Figure 7.2: Band structure with a) U=0, b) U=2 and c) U=10 showing the splitting of the adatom bands, with n=0.3 and tiling 6x6.

Zone path along which k-points were sampled [83].

We then include hybridisation between impurity and surface, shown in Fig. 7.3. At U=2 the band structure displays "shadow bands" characteristic of hybridisation and the spectral function also displays broadening of the upper impurity band. When U=10 we see these effects disappear indicating a reduction in hybridisation between the surface and impurity, as expected since the energy cost of hopping to the half filled impurity site is prohibitive.

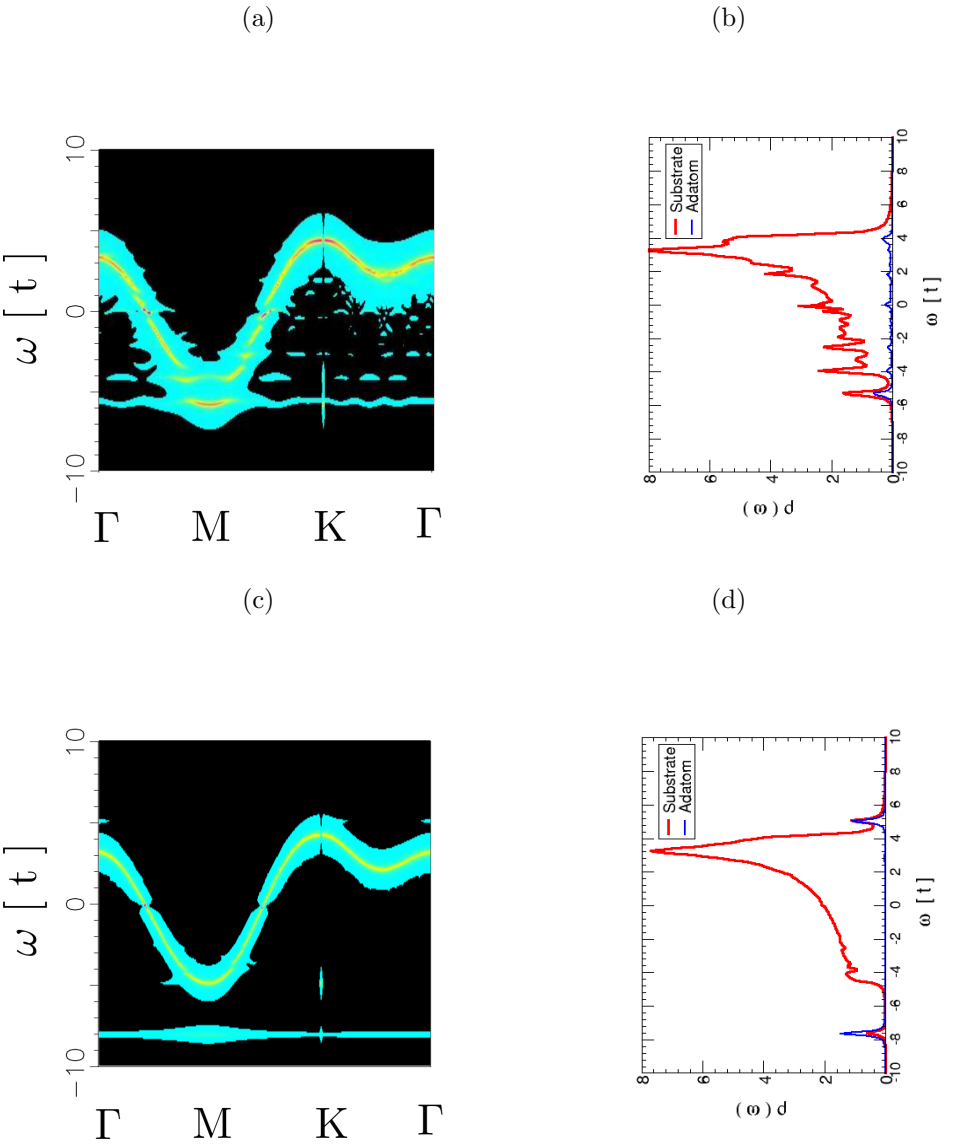

Figure 7.3: Band structure and spectral function from H1 showing hybridisation of substrate and adatom bands at a) b) U=2, and reduction in this interaction at c) d) U=10. Done for n=0.3 and tiling 6x6.

In Fig. 7.4 we show in addition how the band unfolding process is used to uncover the existence of shadow bands in both the band structure and Fermi surface.

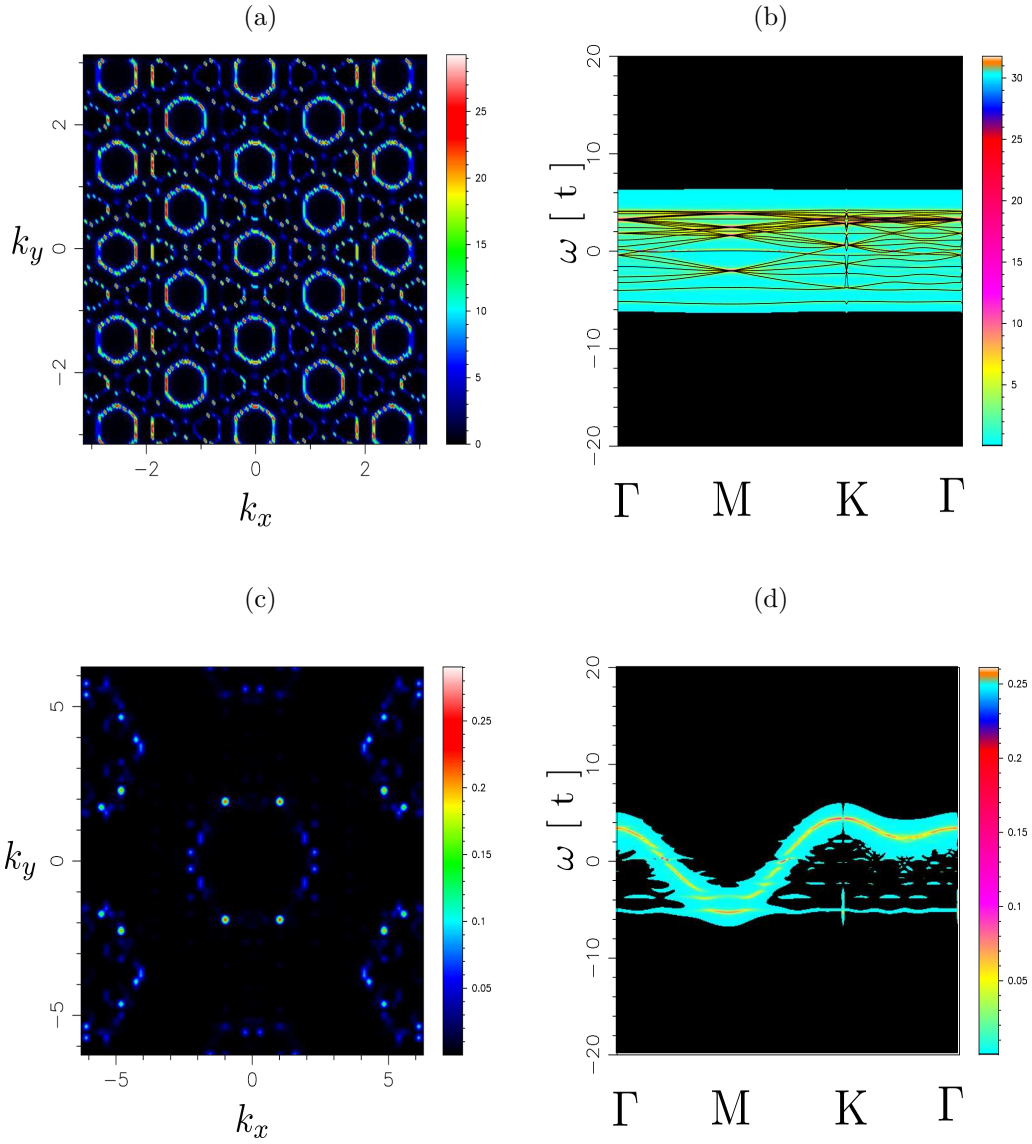

Figure 7.4: Fermi surface and band structure for a 5x5 tiling with U=2, a) b) folded and c) d) unfolded, at a density of n=0.3.

In Fig. 7.5 we further see the effect of increasing U to reduce the hybridisation, this time demonstrated through the Fermi surface.

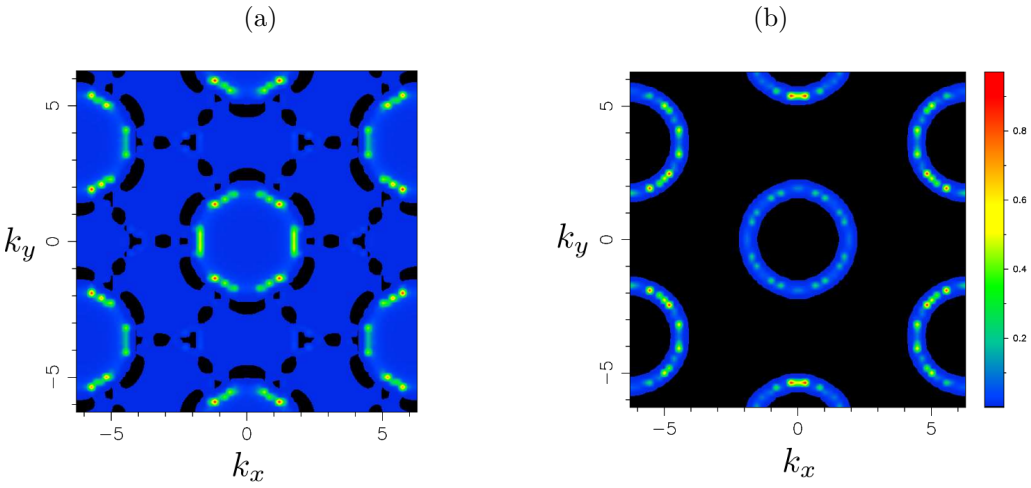

Figure 7.5: Fermi surface of a 2x2 tiling with a) U=0 and b) U=12 at a density of n=0.3. Increasing U reduces the presence of shadow bands.

7.3 Effect of adatom separation

Fig. 7.6 demonstrates through the Fermi surface that the effect of hybridisation is also reduced by increasing the adatom separation, since this corresponds to a reduction of the adatom density and their effect on a comparatively increased conduction band state is subsequently smaller.

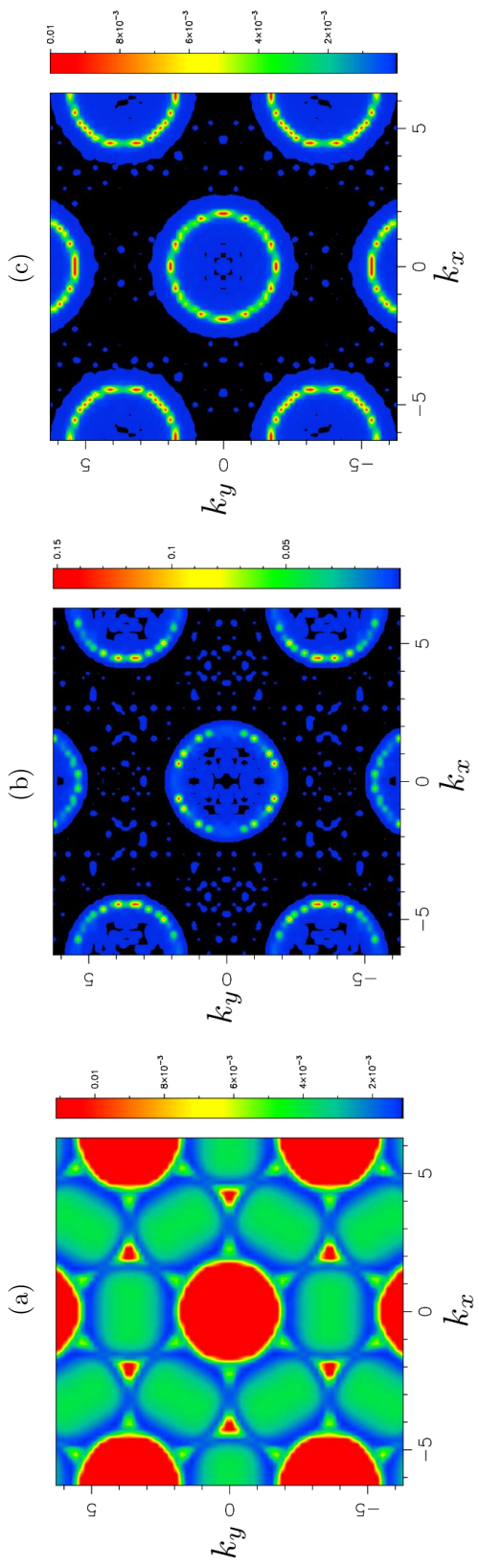

Figure 7.6: Fermi surfaces of a) 2x2, b) 6x6 and c) 11x11 tilings with U=0, at n=0.3. Increasing tiling reduces the presence of shadow bands.

7.4 Effect of impurity level

We considered two values for the impurity level, $E_{Ad} = -2, -6$, and the spectral function below demonstrates the effect this has on the hybridisation using the H1 impurity solver. It also helps illustrate our choice of the latter for later results which necessitates at this point the introduction of the ionic potential to fully explain this.

To begin with in Fig. 7.7 we show the tight binding result, where as observed and in previous work the 11x11 surface state is shown to exhibit a gap opening due to the presence of the ionic potential $V_{Ad} = -3$. Our choice of impurity level below will depend upon maintaining this feature once hybridisation with a correlated impurity has been introduced.

(a)

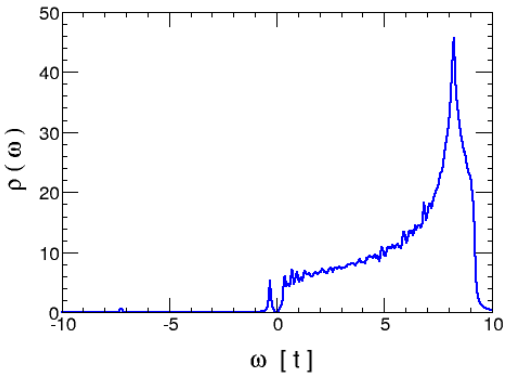

Figure 7.7: H1 spectral function of the surface states for the observed 11x11 tiling with $V_{Ad} = -3$ and a total density n=0.02, with no hybridisation leaving the tight binding result.

Fig. 7.8 shows that by reducing the impurity level we can actually reduce the hybridisation between the impurity and surface, by making it more

energetically favourable to fill the impurity and consequently increase the effect of U repulsion. This is evident since with $E_{Ad} = -2$ we see some surface state levels pinned to the lower Hubbard band but with $E_{Ad} = -6$ these separate and instead leave the surface state which matches that shown above, with a band gap induced by the ionic potential.

From this point we therefore use $E_{Ad} = -6$, since we know that with a reasonable Coulomb repulsion value of U=10 it is possible to regain behaviour qualitatively similar to that observed in Ref. [2], while using $E_{Ad} = -2$ may necessitate an unreasonably large U in order to suppress hybridisation. Additionally since these results used the H1 solver, where the hybridisation has been included in only a simplistic manner as we discussed in our theoretical treatments, we can infer this problem would be compounded when using ED and including the hybridisation is a self consistent way.

These results also reiterate that this system has charge transfer rather than Mott characteristics, where the surface states can exist between the Hubbard bands even with hybridisation.

Using $E_{Ad} = -6$ we can now also consider the effect of U again in Fig. 7.9 and it is clear that with a value of U=2 the hybridisation is not sufficiently suppressed to allow the opening of the gap, in a similar manner to $E_{Ad} = -2$ when U=10. This is an example of the complexity of this system and how there are many contributions that determine its behaviour.

(a)

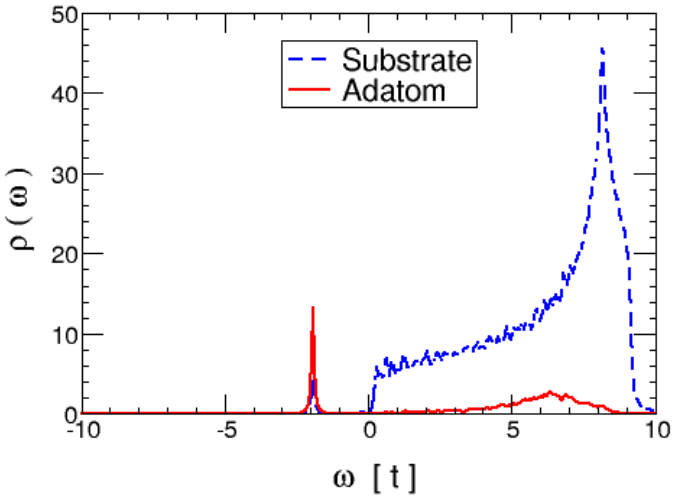

(b)

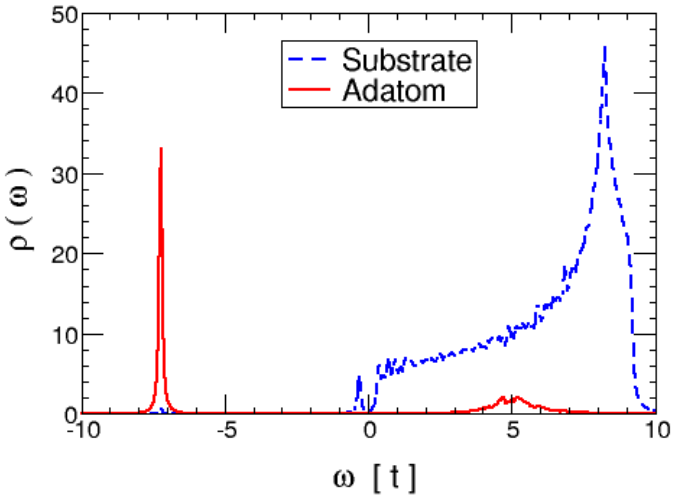

Figure 7.8: H1 spectral functions of the surface and adatom states at two values of a) $E_{Ad} = -2$ and b) $E_{Ad} = -6$ for the observed 11x11 tiling. It can be seen that only with the latter value do we observe the expected gap, hence this is the value we will use henceforth. The adatom spectral functions here have been scaled up by an arbitrary factor so that they can be seen more easily alongside those of the surface state.

(a)

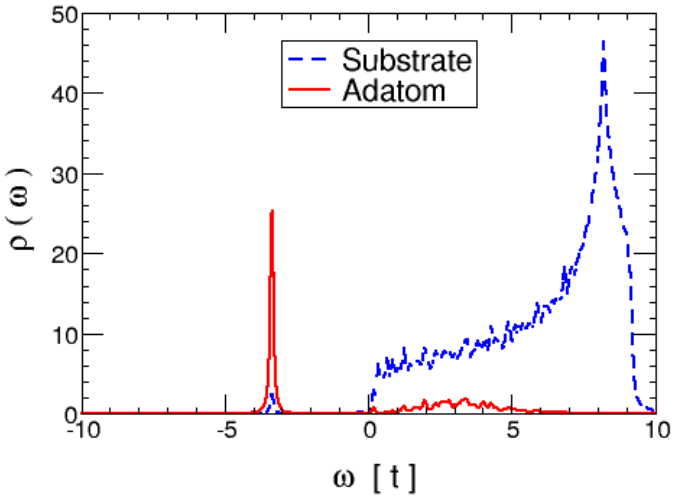

(b)

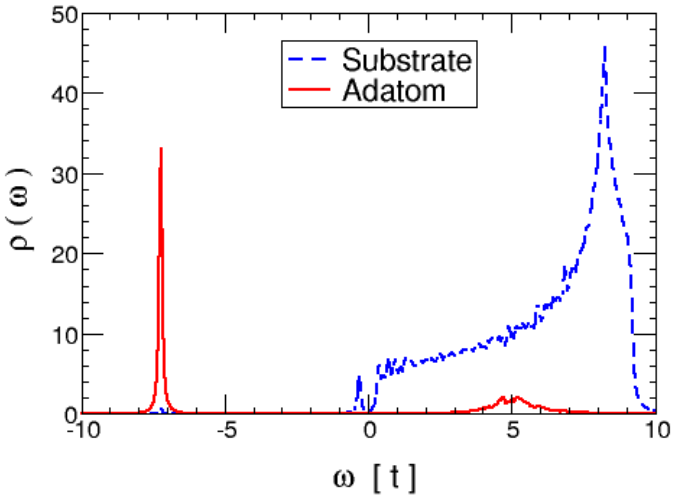

Figure 7.9: H1 spectral functions of the surface and adatom states at two values of a) U=2 and b) U=10, with $E_{Ad} = -6$ for the observed 11x11 tiling. It can be seen that only with U=10 do we observe the expected gap, another example of how high U is needed to suppress hybridisation. The adatom spectral functions here have been scaled up by an arbitrary factor so that they can be seen more easily alongside those of the surface state.

7.5 Impurity localised by correlation

Although our work moves beyond the tight binding approximation, it should exist as the high U limit of the AIM, and testing this serves as a good vindication of our model and the parameters we have chosen. In the previous section we chose our impurity level such that we were confident a gap would exist at high U and here we show in Fig. 7.10 that at extreme values of U both the H1 and ED solvers converge on the tight binding result. This is expected since at large enough values of U the strongly correlated impurity becomes essentially isolated and purely localised, due to the energy cost meaning there is no longer any hybridisation and this leaves only the ionic potential to effect the substrate.

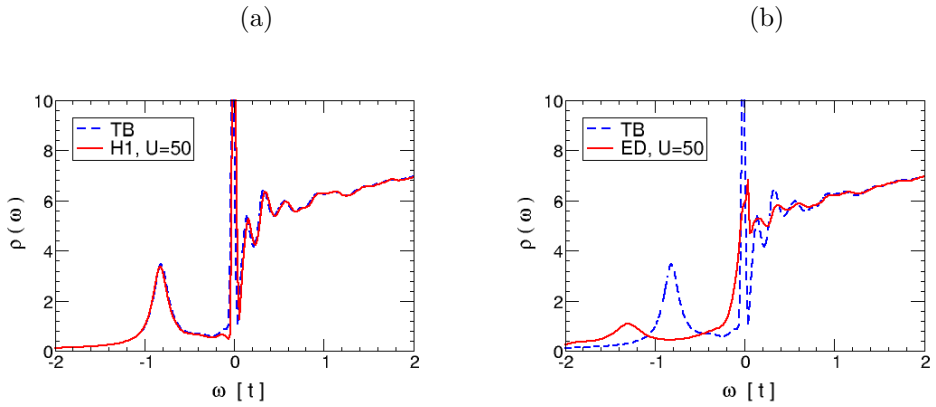

Figure 7.10: Substrate DOS for the TB model shown with the a) H1 and b) ED result with U=50 and total density n=0.015. It can be seen that at high U, H1 and ED approach TB, with H1 approaching sooner. It can also be seen that this low total density is close to the gapped state observed in experiment [2].

7.6 Phase diagram of super-lattice systems in the strong coupling regime

Having tested the limits and parameter dependence of H1, we performed runs at a variety of total electron densities and adatom separations, using the results to create an initial picture of the phase diagram for super-lattice systems. Although removed from the real picture in several important ways, such as lacking low temperature effects and hybridisation, it is computationally efficient in its standard form and serves as a benchmark with which to compare more advanced models. The spectral function was inspected to determine what state the system was in and, with this simple inclusion of Hubbard U interactions, we identified three distinct states which are displayed in Fig. 7.11 and Fig. 7.12.

These cases are: that there is mixed impurity-surface state at or below the Fermi level, which we term an apparent gap since the separation of the surface states is due only to hybridisation; that there is a predominantly isolated impurity band below the Fermi level with the surface spectral function at or above the Fermi level, with a gap emerging but above the Fermi level; and a true gap case, where the emergent gap in the surface state becomes situated over the Fermi level with the impurity peak much lower. This gap is due to the ionic potential as in tight binding.

Below we demonstrate the basic effect of the density on these phases within the Hubbard 1 approximation, by looking at points along a line

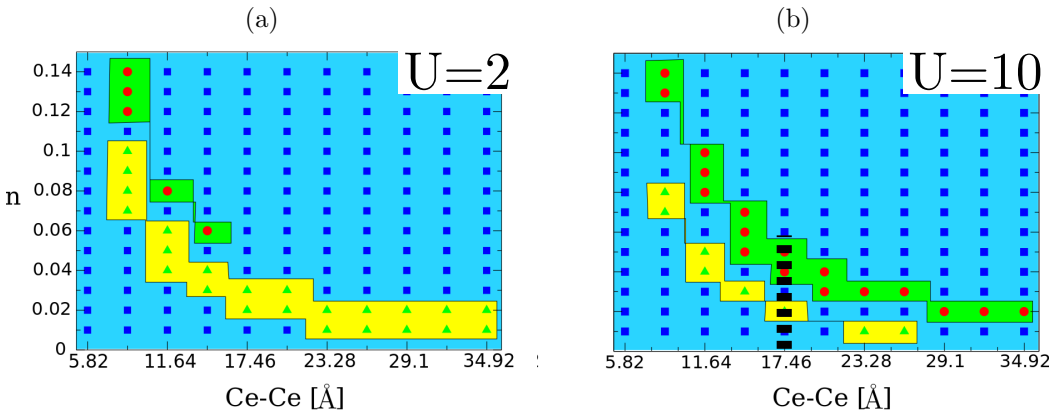

Figure 7.11: Phase diagram of the system for a) U=2 and b) U=10. The background of squares represent cases where no gap was observed; the upper regions of circles denote true insulating band gaps due to ionic potential V_{Ad}; lower triangles regions indicate apparent gaps due to presence of impurity. The black line indicates the line of points for whose spectral functions are shown in Fig. 7.12

from the above phase diagram at a fixed adatom separation of 17.46 Å corresponding to a 6x6 tiling with U=10. It can be seen at low densities that the lower band contains overlapping surface and adatom states. As we increase the total electron density we move the Fermi energy up to the edge of the surface spectral function with the lower bands now far below this point and exhibiting reduced hybridisation. If we increase the density further then there exists a clear gap in the surface states. This trend also exists for fixed density while we increase the tiling, since the effect of both is to increase the electron number in the system.

It is the impurity occupation which determines these characteristics of the spectral function. If the impurity is below half filling then it hybridises quite freely with the surface states. As it approaches half filling, the impact of U

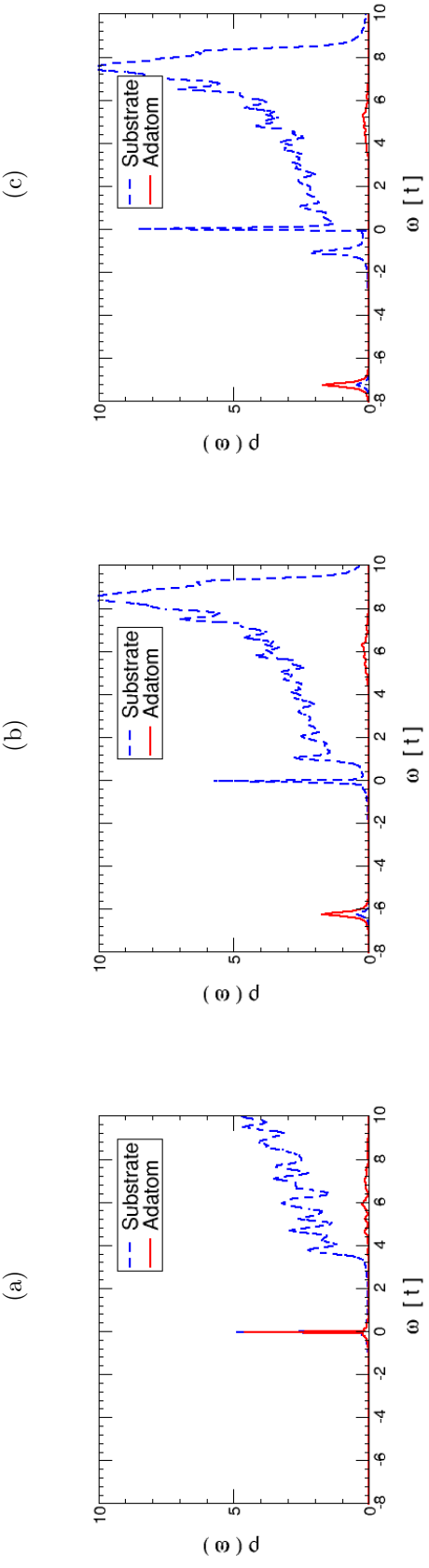

Figure 7.12: A line on the H1 phase diagram, showing the substrate and adatom DOS at an adatom separation of 17.46 Å for densities a) 0.02, b) 0.03 and c) 0.04 and U=10. It can be seen that at low n the substrate and adatom hybridise around the Fermi level. As the density and hence the number of electrons in the system increases we see that first the adatom becomes half filled and separates. A gap also opens in the surface spectral function due to the presence of V_{Ad} and further increasing the density leads to the Fermi level becoming situated within this gap.

becomes important. At U=10 this leads to a suppression of hybridisation which allows the ionic potential to open a gap in the surface state, and the bottom band of this gap is occupied as we increase density further since the impurity cannot be doubly occupied. When U=2 however, this trend does not seem to persist for all combinations of density and tiling which correspond to a half occupied impurity, suggesting that in many cases hybridisation persists where it doesn't with U=10.

Chapter 8

Intermediate Correlation Regime

8.1 Introduction

We will now focus on results calculated using exact diagonalisation. We will show 2D plots similar in structure to Fig. 7.11, which was based on the Hubbard 1 approximation, but as the phase space is more complicated we will simply show the results for several system parameters rather than defining phases. Results were obtained in the same mass run method as H1, over several total electron densities and adatom separations. We will plot several pertinent parameters against changes in these values, but in some cases also against the impurity electron occupation. These plots include more runs which allow us to show changes as the impurity goes from empty to full, which our original total density spread did not cover. As well as 2D colour plots we will also employ simpler line graphs, which in some cases communicate our findings better. We will begin by discussing results in isolation, but at the conclusion of this chapter will consider them together in order to draw conclusions.

8.2 Charge Localization Properties

8.2.1 Effect on impurity occupation

In Fig. 8.1 we show plots of the impurity occupation as calculated by ED at two values of U, as the total density and adatom separation is varied along the axes. Each plot has been given the same maximum value to allow comparison.

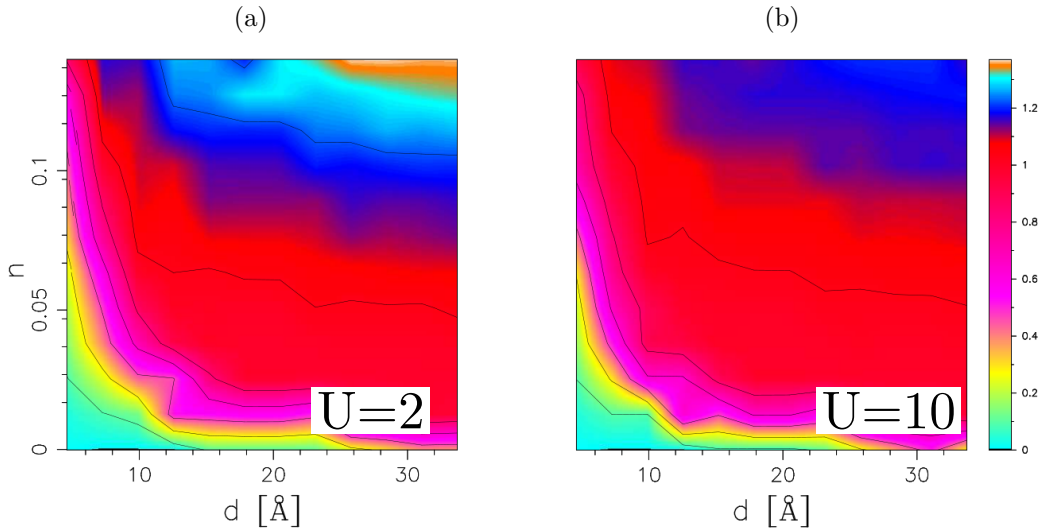

Figure 8.1: 2D colour plots showing how the impurity density changes with adatom separation and total electron density for a) U=2 and b) U=10, as calculated with ED.

It can be seen that the impurity becomes rapidly filled as we increase the density of electrons in the system until it reaches half filling. At this point, growth in occupation slows down considerably and with U=10 the impurity site shows more resistance to occupation beyond half filling than with U=2. These observations are as expected, since the impurity level

has the lowest energy in the system and it would be favourable to occupy this first. That is until half filling, at which point the energy cost of double occupation associated with U favours filling the conduction band and leaving the impurity occupation unchanged. Of course, there is still hybridisation and these calculations are done at finite temperature, meaning that the impurity occupation does still fluctuate and, on average, increases.

It is also clear from these plots that our initial spread of total electron densities does not cover the whole range of impurity occupations, which is maxing out around half filling after becoming occupied rapidly. This is a consequence of our method where we impose a total electron density in our system and fill an empty impurity and conduction band until this is reached, rather than choosing a total number of electrons. This is why there is also an increase in the impurity occupation as the adatom separation increases, because there are correspondingly more surface atoms in the unit cell, more electronic states to fill and so at a fixed fractional occupation there will be more electrons.

8.2.2 Effect of correlation - the Z function

Here we show 2D plots of the quasi-particle re-normalisation weight [84], or Z function, calculated in ED at U=2 and U=10 for each combination of density and adatom separation. The Z function is calculated from the self energy and inversely proportional to electron effective mass, therefore it maximises at 1 in a conducting system without strong correlation effects, and approaches zero as correlation leads to higher effective masses and insulating behaviour.

$$Z^{-1} = 1 - \frac{\partial Re\Sigma(\omega)}{\partial\omega}\Big|_{\omega=\omega_0} \propto \frac{m*}{m} \tag{8.1}$$

These results show the complex changes undergone in the system as electron and density and adatom separation are changed, with numerous regions indicating strongly correlated behaviour which expand or emerge as we increase U.

We can also show the change in Z with respect to the impurity occupation. This allows us to include a larger range of occupations up to complete filling.

While colour plots are helpful in giving an overview of parameters changes, simpler line graphs taken at just a few values can more clearly indicate some features. This is especially true for the Z function, as while it can be discerned from the 2D graph that at U=10 there are two horizontal regions where it tends to zero, they are not entirely distinct and it is not clear what

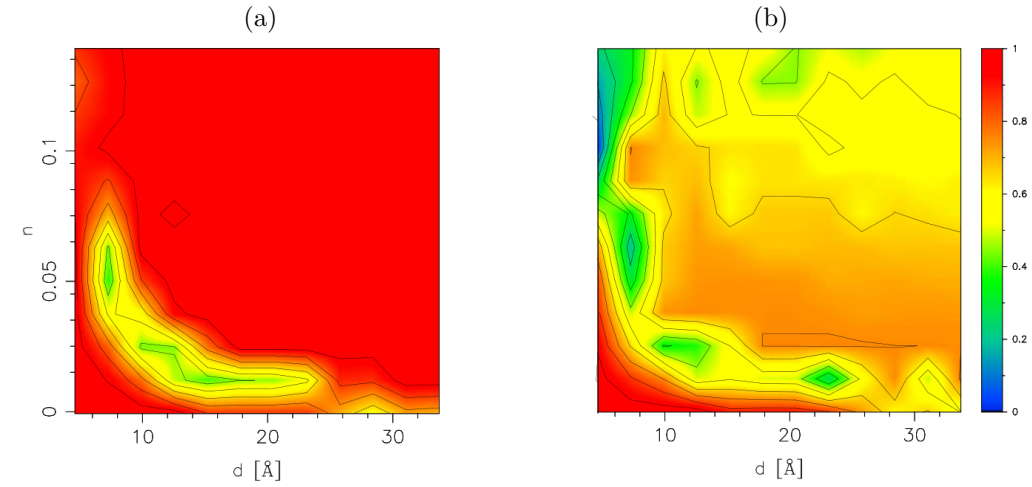

Figure 8.2: 2d colour plots of Z-function from ED calculations at a) U=2 and b) U=10 shown in relation to the total system density.

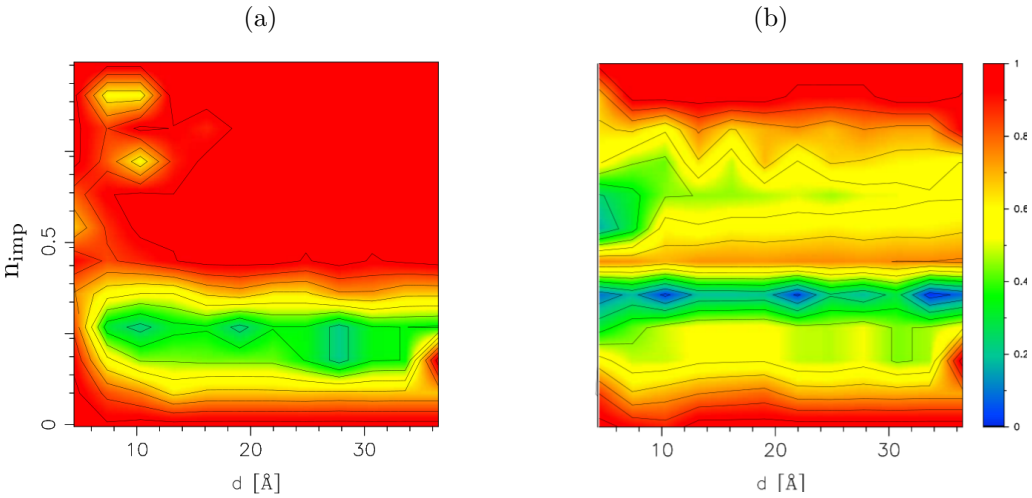

Figure 8.3: 2d colour plots of Z-function from ED calculations at a) U=2 and b) U=10 shown in relation to the impurity density.

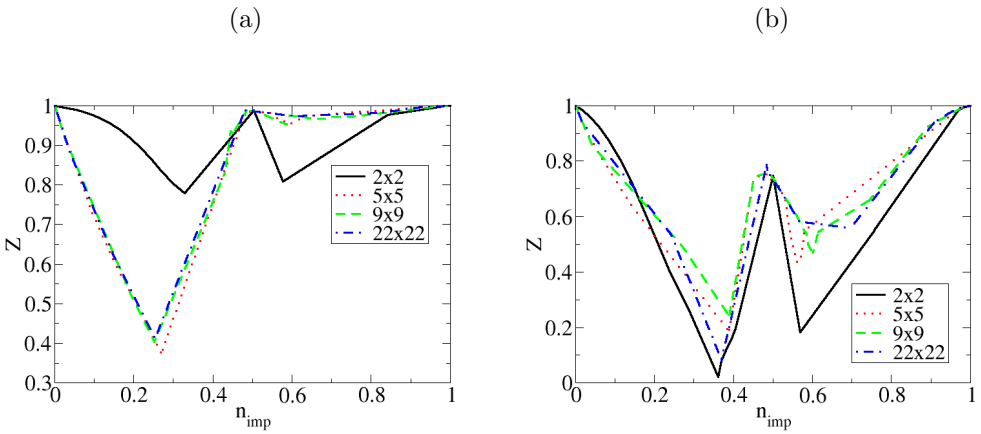

Figure 8.4: The Z function for a) U=2 and b) U=10 shown at a range of adatom separations.

happens between them around n=1. The behaviour becomes much clearer when we simply look at a line graph of Z against the impurity density, which we show below for the smallest and largest considered adatom separations and for a variety of U values.

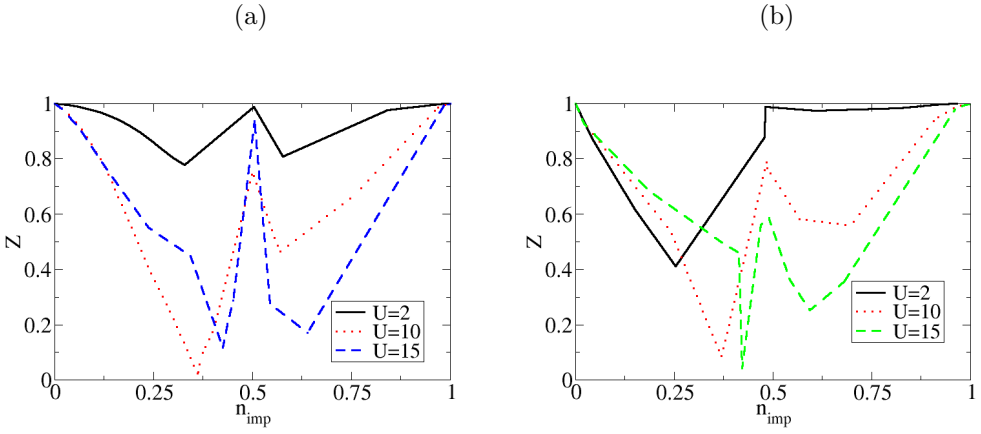

Figure 8.5: Line plots of Z against n_{imp} at tiling a) 2x2 and b) 22x22 for U=2,10,15 and $V_{ad} = -3$. A similar trend can be seen at both tilings that an increasing U leads to the growth of a second correlated region above half filling.

It can seen that there are clearly two regions of low Z indicating strongly

correlated behaviour which become in general more pronounced as U increases. They exist at both small and large adatom separation, except for the second region at low U and large tiling. The central maxima at half filling is also reduced at large tiling.

These cases differ from what we would expect as a typical result, which is that when the impurity is empty or full then Z = 1, indicating a lack of strongly correlated behaviour, and that Z would tend to 0 near half filling as a single minima, which is where the effect of U will be at its maximum. Instead at high U we see this two minima structure, where Z actually peaks again around half filling, suggesting reduced effect of U. As we reduce U the second minima reduces, which is particularly evident in the largest tiling case, and we can see the system approaching typical behaviour again, but with a major minima that is offset from half filling.

We can glean further insight by considering how Z changes in relation to the total electron density, as well as comparing it to the impurity occupation and impurity spin, which is shown in Fig. 8.6 for two values of U. By considering the 2x2 tiling we can also easily translate the total electron density into actual electron number, knowing that it contains 10 electron states in total. It can be seen then that the first minima of Z corresponds to having a single electron in the system and the second to having three. The maxima occurs when there are two electrons which coincides with the impurity becoming half full. Also, the first minima coincides with the maxima of the impurity spin and the maxima to a small in the spin, even though

the impurity occupation has increased.

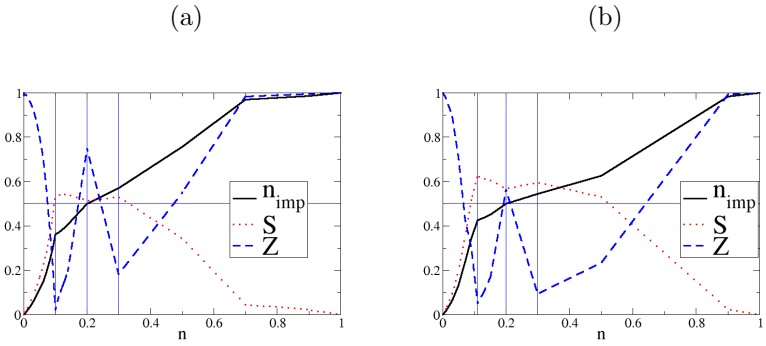

Figure 8.6: Line plots of impurity occupation, S and Z against total density at tiling 2x2, for a) U=10 and b) U=15 with $V_{Ad} = -3$. Lines have been added to highlight the densities corresponding to minima and maxima in Z, and make it clear how these coincide with impurity occupation and spin. It can be seen that increasing U generally increase correlation, showing as a decrease in the Z function minima and central peak, but the overall behaviour remains unchanged.

In Fig. 8.7 we show the spectral function at densities corresponding to the extrema of Z for 2x2 and U=10.

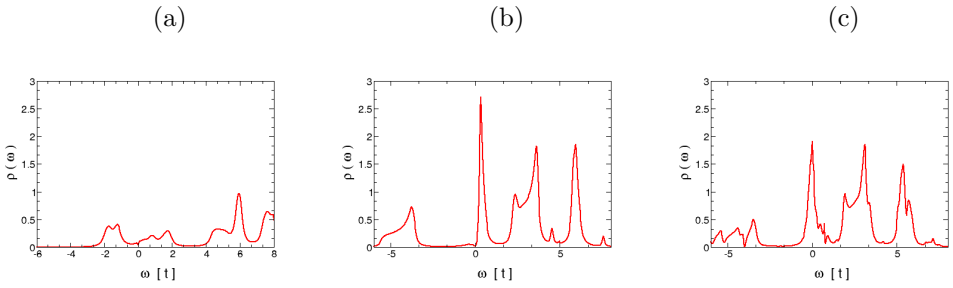

Figure 8.7: Spectral functions for the smallest 2x2 tiling, shown at total densities corresponding to the extrema of the Z - function a) n=0.1, b) n=0.2 and c) n=0.3 with $V_{Ad} = -3$ and U=10.

To try and understand the significance of these results we focus on the small 1x1 tiling and also consider the effect of setting $V_{Ad} = 0$, which is

shown in Fig. 8.8. It is clear that the ionic potential does have an effect on this behaviour since it modifies the position of the minima, although there do appear to still be two. However the first minima now occurs at half filling, while the second is just a small perturbation at higher occupancy.

(a)

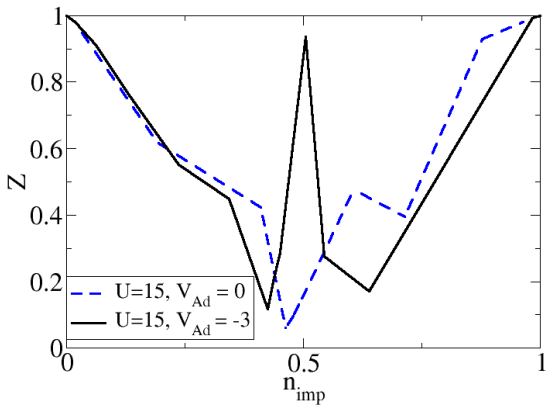

Figure 8.8: Line plots of Z against n_{imp} at tiling 2x2 with U=15 and for $V_{Ad} = -3, 0$. It can be seen that the two-minima structure is modified by the presence of the ionic potential.

If we compare the U=15 case with $V_{Ad} = 0$, shown in Fig. 8.9, we can see that although the features are modified the minima and maxima do occur at the same electron densities with V_{Ad}, and the first minima again coincides with the maxima of the spin S. However the impurity spin no longer has a dip at n=0.2 to coincide with the maxima of the Z function, and the impurity occupation reaches half filling between n=0.1 and n=0.2. The major change however is the reduction in the second minima, which while still being present indicates there is a lesser level of strong correlation when not in the presence of the ionic potential.

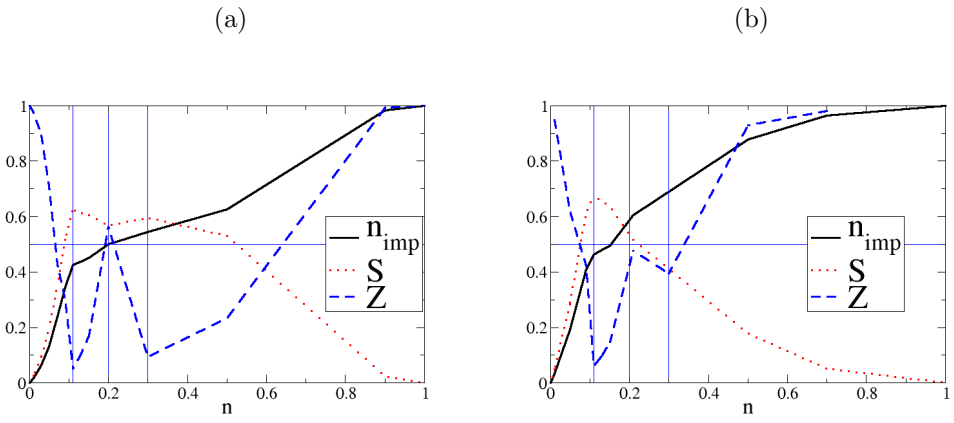

Figure 8.9: Line plots of impurity occupation, S and Z against total density at tiling 2x2, for U=15, a) $V_{Ad} = -3$ and b) $V_{Ad} = 0$. Lines have been added to highlight the densities corresponding to minima and maxima in Z, and make it clear how these coincide with impurity occupation and spin. Removing the ionic potential causes the Z function to collapse to a single minima, coinciding at the same occupation as the first minima with $V_{Ad} = -3$, suggesting it is the second minima state that disappears.

In Fig. 8.10 we show the spectral functions and band structure for the 2x2 tiling with U=15 and $V_{Ad} = -3$ as the total densities 0f n=0.1,0.2 and 0.3 which correspond to the first minima, maxima and second minima of Z respectively. In Fig. 8.11 we compare the n=0.1 point to that for $V_{Ad} = 0$ to demonstrate that the observed structure is comparable and showing the same behaviour. The x-axis again displays the Brillouin Zone path along which k-points were sampled [83].

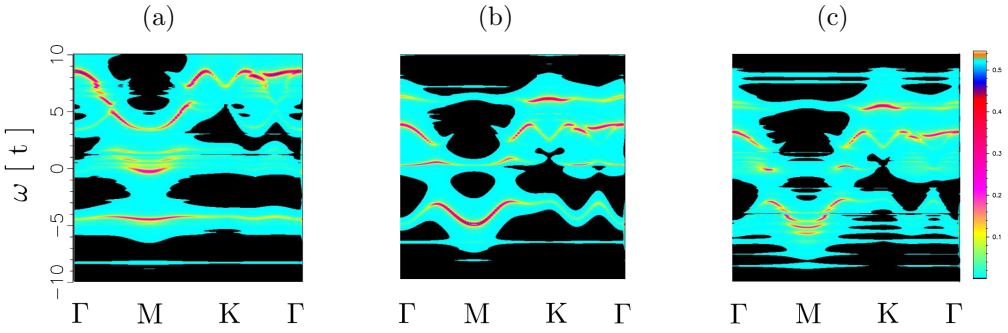

Figure 8.10: Band structure for the smallest 2x2 tiling, shown at total densities corresponding to the extrema of the Z - function at a) n=0.11, b) n=0.2 and c) n=0.3 with $V_{Ad} = -3$.

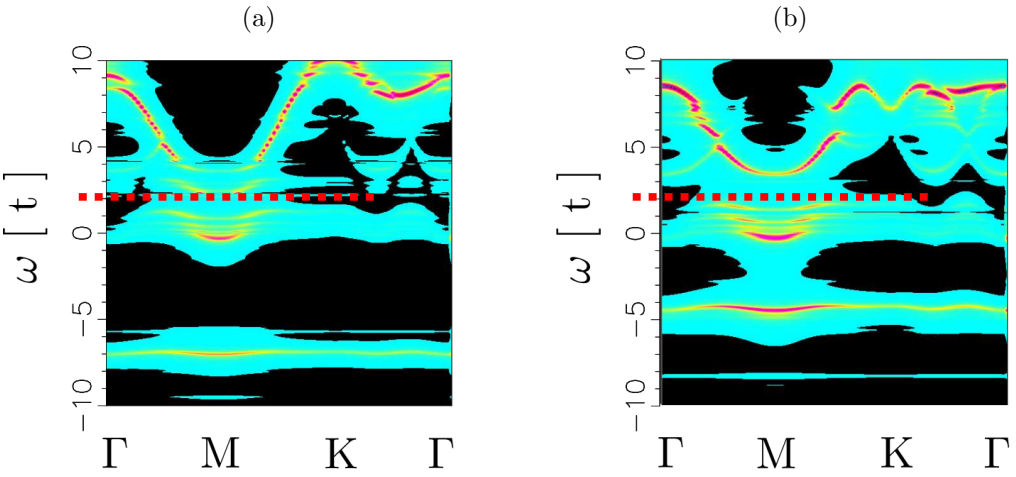

Figure 8.11: Band structure for the smallest 2x2 tiling, shown at the total density corresponding to the first extrema of the Z - function at n=0.11 with a) $V_{Ad} = 0$ and b) $V_{Ad} = -3$. It can be seen that the band structure around the Fermi level, as indicated by the dashed lines, in these two cases is comparable, reinforcing the conclusion that it is the first minima state is the same in both cases.

8.3 Magnetic Properties

8.3.1 Effect of impurity spin

In this section we focus on how numerous magnetic properties, such as the impurity spin and its susceptibility, change as total density and adatom separation are varied. In Fig. 8.12 it can be seen that the growth of the impurity spin with total electron density shows a similar trend to the impurity occupation in Fig. 8.1. This is expected since as the impurity occupation increases up to half filling the spin on that site will also increase to a maximum. While at low densities U=2 and 10 are similar, they diverge as this increases, with the impurity attaining higher spins overall with U=10.

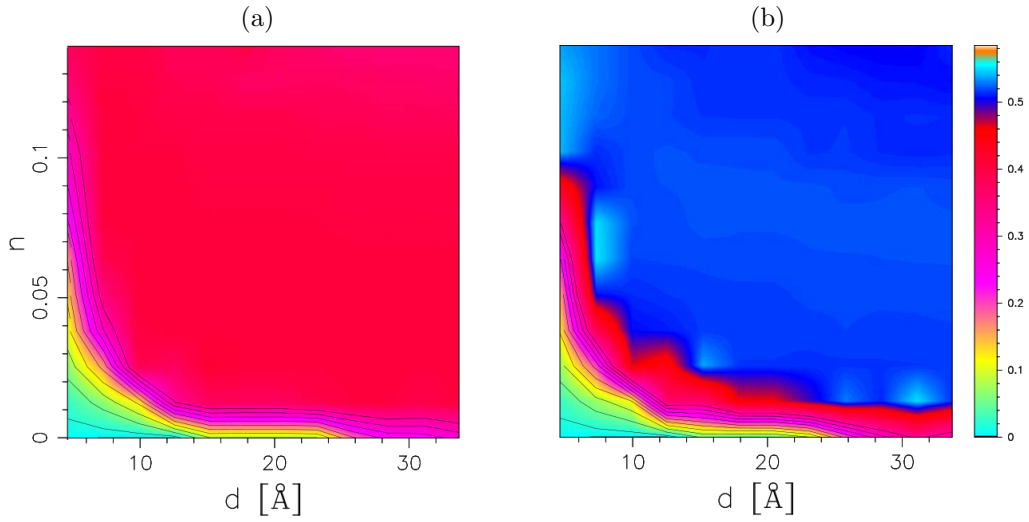

Figure 8.12: 2d colour plots of the total impurity spin at a) U=2 and b) U=10 shown in relation to the total system density and adatom separation.

Fig. 8.13 displays the impurity spin in relation to the total impurity occupation and adatom separation, also showing that with U=10 the impurity

attains a higher spin. But they also demonstrate that when the impurity is empty or full the total spin goes to zero, with a gradual rise in between until it peaks near the centre, although it is notably offset from half filling. This was noted also in the previous chapter, when the spin was shown alongside the Z function, and it instead lines up well with the first region of strong correlation shown in Fig.8.3 (b).

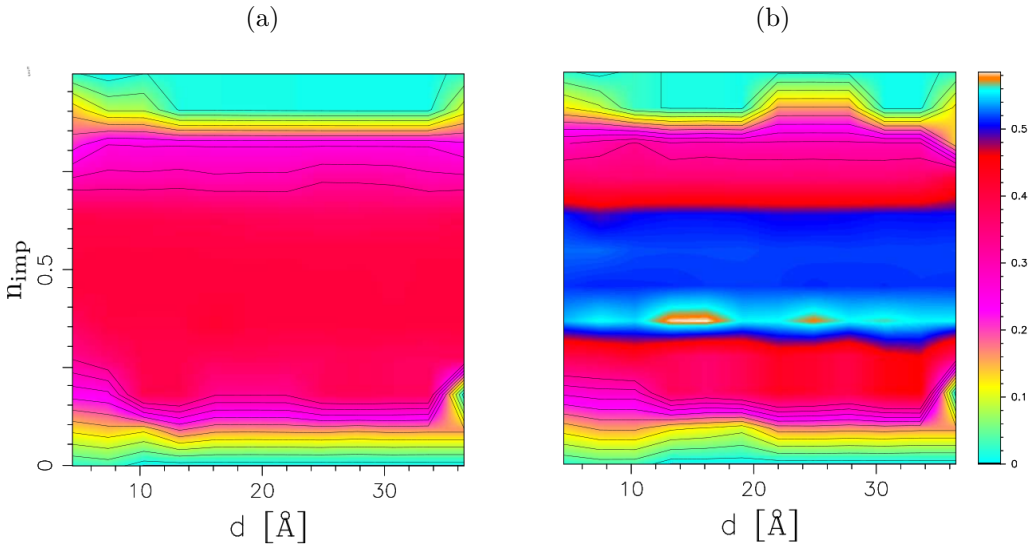

Figure 8.13: 2d colour plots of the total impurity spin at a) U=2 and b) U=10 shown in relation to the impurity density and adatom separation.

These plots also suggest that the impurity spin does not significantly vary with adatom separation, since they remain fairly uniform as you track them along the x-axis. This is made clearer in Fig. 8.14 where we show how the spin varies with impurity occupation for U=2 and U=10 at the extreme values of adatom separation corresponding to a 2x2 and 22x22 unit cell tiling. The fact that at such different separations the impurity spin remains nearly identical suggests it is a purely local quantity and is unaffected by

the larger system, perhaps because it is screened.

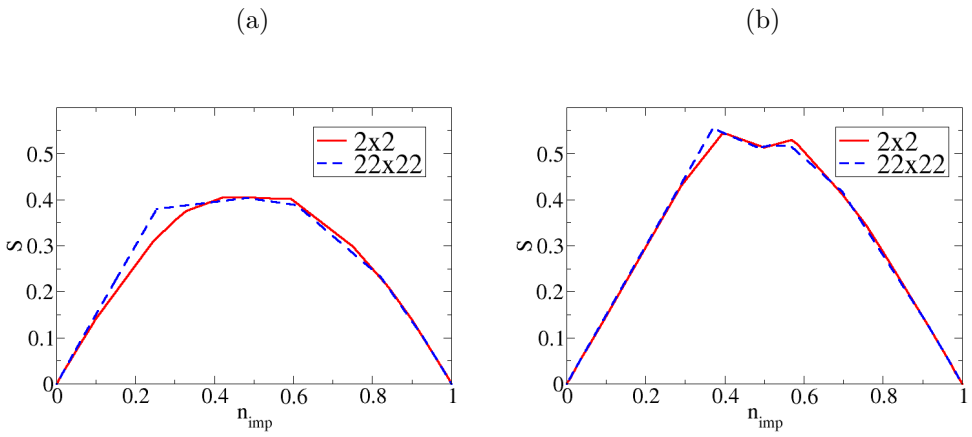

Figure 8.14: Here we show the total impurity spin against impurity density, for the smallest and largest adatom separations with a) U=2 and b) U=10. It is clear from this that even at different scales, the impurity spin behaves the same with regards to the impurity density.

8.3.2 Effect on magnetic susceptibility

We have performed calculations on large 22x22 tilings in an effort to include the extreme limit of our system which is comparable to a Kondo lattice of independent magnetic impurities. We want to test whether Kondo effects do in fact arise in this limit, but encounter issues in determining it. The main signature of Kondo which we might want to find is the existence of the Kondo resonance in the spectral function at the Fermi level, however we determined after numerous tests that such a feature may not be identifiable in our case. This is due to our plotting of the spectral function incorporating a broadening factor to ensure a more continuous function rather than singular peaks. This broadening is small around the Fermi level to ensure that we do not wash-out any features such as a gap, but this also means any weight at the Fermi level has an exaggerated peak structure which makes it impossible to distinguish a Kondo peak.

Instead, we attempt to detect Kondo behaviour by calculating the magnetic susceptibility χ [40], which at low temperature is much reduced by the Kondo effect [85]. Using an adatom separation of 64 Å, or a 22x22 tiling, we show in Fig. 8.15 how the magnetic susceptibility χ changes with impurity occupation. It can be seen that it goes to zero for an empty or full impurity, is close to zero at low occupation but then grows to be maximised between half and three-quarter filling, suggesting the existence of Kondo behaviour at impurity occupations below half filling.

(a)

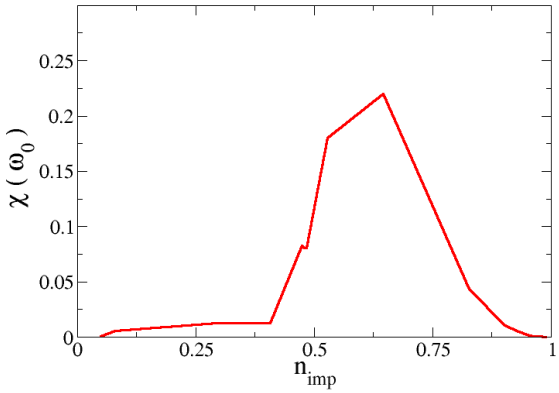

(b)

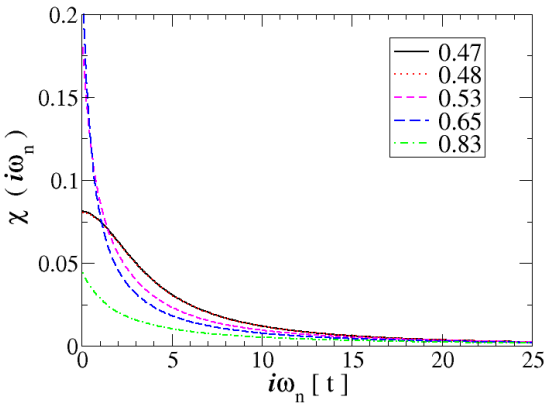

(c)

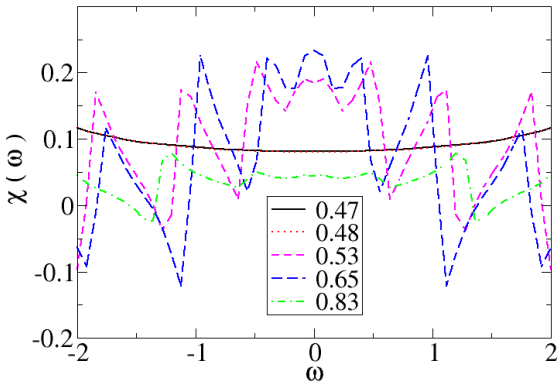

Figure 8.15: Plots showing χ at a range of adatom occupations at the largest 22x22 tiling, evaluated at a) ω_0 and plotted on the b) imaginary and c) real axis for a selection of those occupations.

In Fig. 8.16 we show $\chi(\omega_0)$ at both the 2x2 and 22x22 tilings. While they show similar behaviour at large impurity filling they differ greatly at low occupation, although 2x2 does exhibit a region of possible Kondo behaviour around a filling of $n_{imp} = 0.4$, which coincides well with the first minima of Z.

(a)

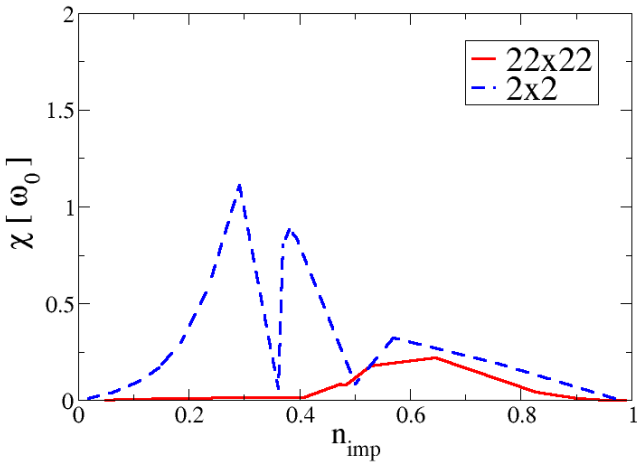

Figure 8.16: Plots showing χ at a range of adatom occupations at the largest and smallest tilings, evaluated at the first Matsubara frequency ω_0.

8.3.3 Effect of inter-adatom interactions - RKKY

We performed a preliminary CDMFT [52] [67] calculation for a cluster of 4 impurities with a variety of adatom separations, with the cluster shown as an inset on Fig. 8.17. This allows us to model indirect surface-mediated magnetic interactions between the impurities, in other words RKKY physics. However upon inspection we discovered that the calculations did not converge, as evidenced by the densities of the four impurity sites included in the unit cell not being equal. We believe this occurred because the number of reciprocal space points used was not sufficient for periodic boundary conditions to be properly instituted. A smaller number of reciprocal lattice points was necessary due to memory limitations, since the real space unit cell modelled is necessarily larger to incorporate several impurities.

However, the calculations did complete and show that in principle our model is able to compute inter-adatom interactions. We show in Fig. 8.17 the results, which still exhibit RKKY-like correlation between neighbouring impurity spins where variation of the adatom separation shows fluctuations between ferro- to antiferro-magnetic behaviour. With greater memory resources to tackle larger arrays the precise role of this interaction could be further investigated.

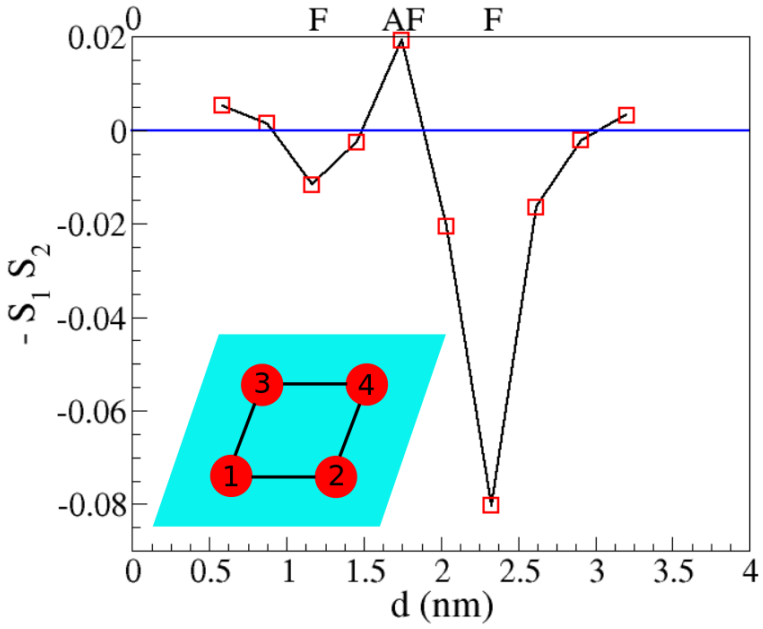

Figure 8.17: Initial RKKY results, showing the distance-dependent exchange interaction between magnetic moments S_1 and S_2 as adatom separation d is varied. The sign of the implicit oscillatory coupling energy J_{12} ($-S_1S_2 = -J_{12}S_1S_2$) determines whether the magnetic ordering is antiferro- or ferro-magnetic [9].

8.4 Effect of density and tiling on the spectral function

Similarly to what we did for H1, we would like to identify some particular phases and trends exhibited by the ED modelled system which more properly takes into account the hybridisation.

To begin with we compare some ED results in a similar fashion to those done with H1, this time considering a fixed total density of n=0.3 at the three smallest tilings for U=2 and U=10. We find in contrast to H1 that there is a qualitative change in one of the spectral functions as tiling and U are changed, in that for the 4x4 tiling the hybridised band becomes split about the Fermi level for large U.

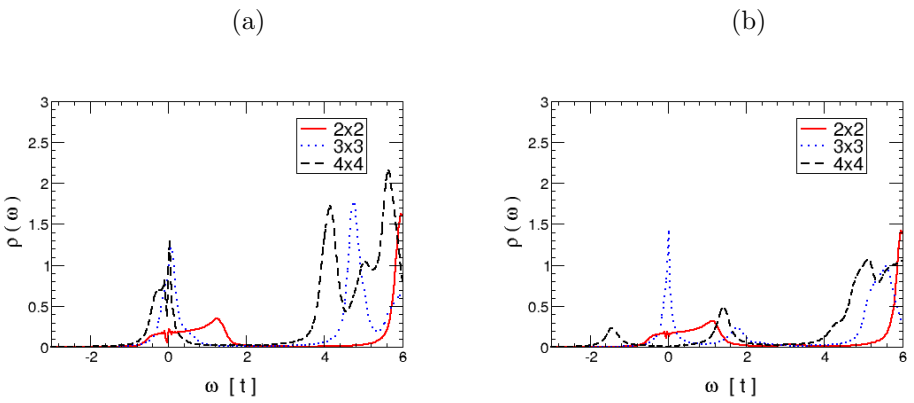

Figure 8.18: The substrate DOS for points along a line in the ED a) U=2 and b) U=10 phase diagram, at total density 0.03 and the 3 smallest adatom separations.

We show in Fig. 8.19 the spectral function at fixed density n=0.05, for U=10 and a selection of tiling. Here we show the adatom and substrate results together so that the relative weighting can be compared. In the first we see that the surface and adatom hybridise with weightings similar on both sides of the Fermi level. In the second, there is a single peak below the Fermi level that has similar weightings of both surface and adatom states. It is only in the third case that we observe a gap existing purely within the surface state, which we attribute to the ionic potential, rather than hybridisation with the impurity band like the previous two.

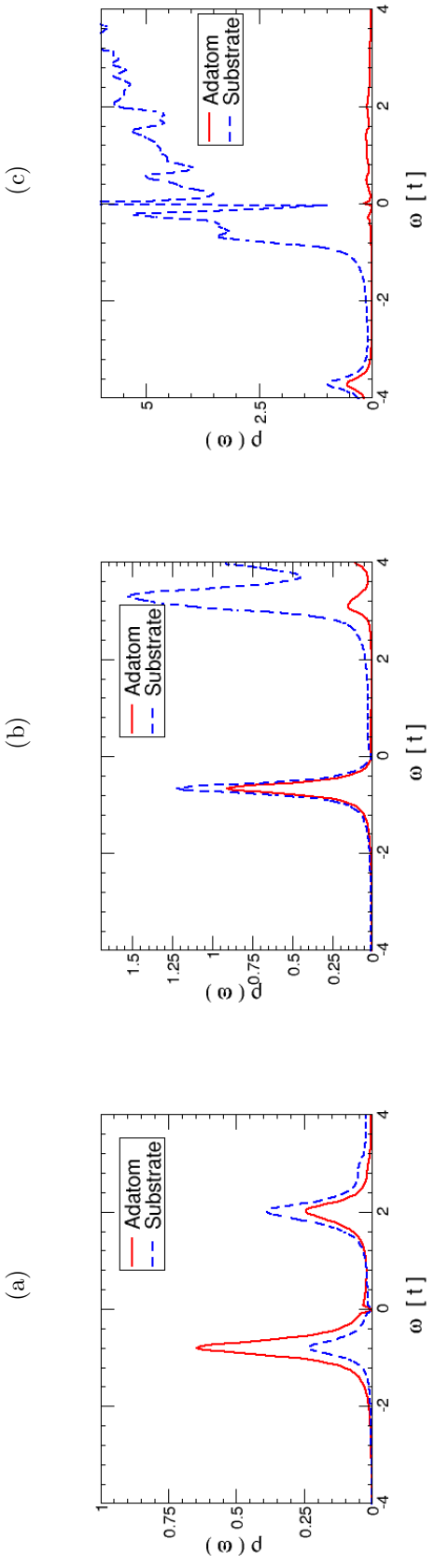

Figure 8.19: Comparison between substrate and adatom DOS for a density of 0.05 and U=10 at tilings a) 3x3 b) 4x4 c) 9x9. Each one represents a distinct behaviour of the system, due to the location and weighting of peaks about the Fermi level. The impurity DOS of the largest adatom separation has been artificially scaled up to make it visible alongside that of the total system, which is in truth several magnitudes larger.

We also consider fluctuations in the spectral function at the Fermi level, calculated as $\rho(E_F) = -\frac{ImG(i\omega_0)}{\pi}$ and shown in Fig. 8.20 for the largest and smallest tilings at U=2 and U=10. In Fig. 8.21 we show this just for $n_{imp} \geq 0.5$ to have a more comparable scale.

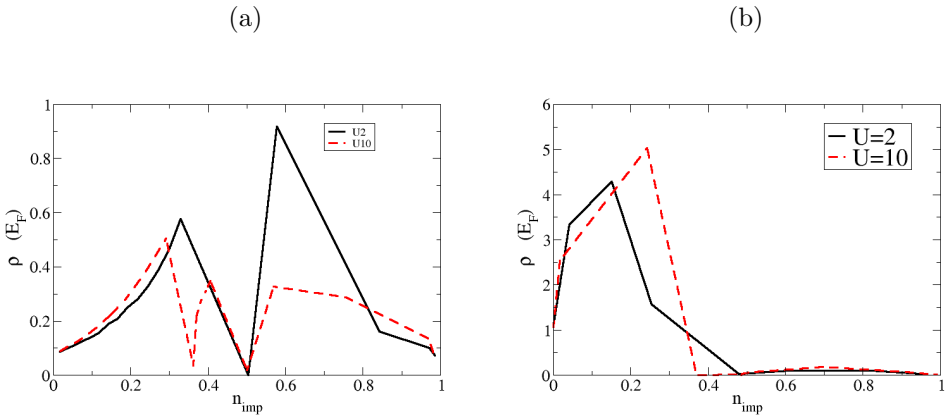

Figure 8.20: The spectral function at the Fermi level, calculated as $\rho(E_F) = -\frac{ImG(i\omega_0)}{\pi}$, as a function of n_{imp} for tilings a) 2x2 and b) 22x22 at U=2 and U=10.

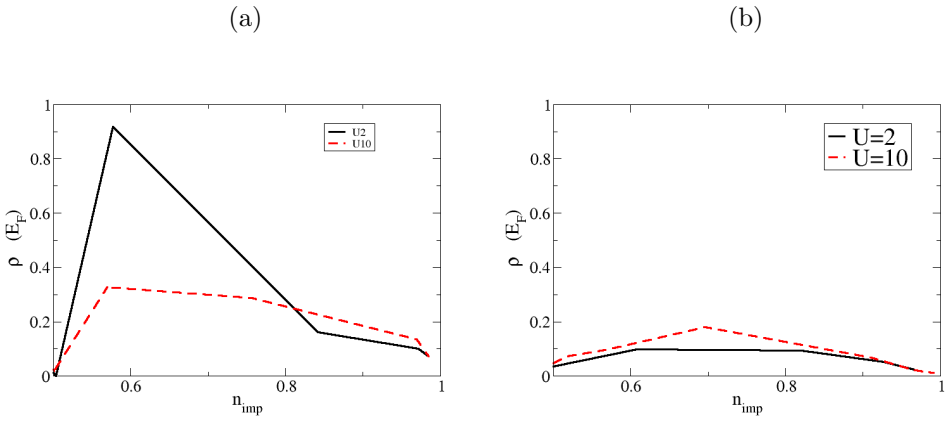

Figure 8.21: The spectral function at the Fermi level for $n_{imp} \geq 0.5$, calculated as $\rho(E_F) = -\frac{ImG(i\omega_0)}{\pi}$, as a function of n_{imp} for tilings a) 2x2 and b) 22x22 at U=2 and U=10.

An interesting feature is for 2x2 with U=10 the weight at the Fermi level

goes to zero at $n_{imp} \approx 0.36$, before increasing again and then falling to zero at half filling. We show this change of behaviour in Fig. 8.22 by showing the spectral function for the point at $n_{imp} \approx 0.36$ and the peak at $n_{imp} \approx 0.4$. It can be seen that the system goes from a charge transfer like gap into a Kondo like peak.

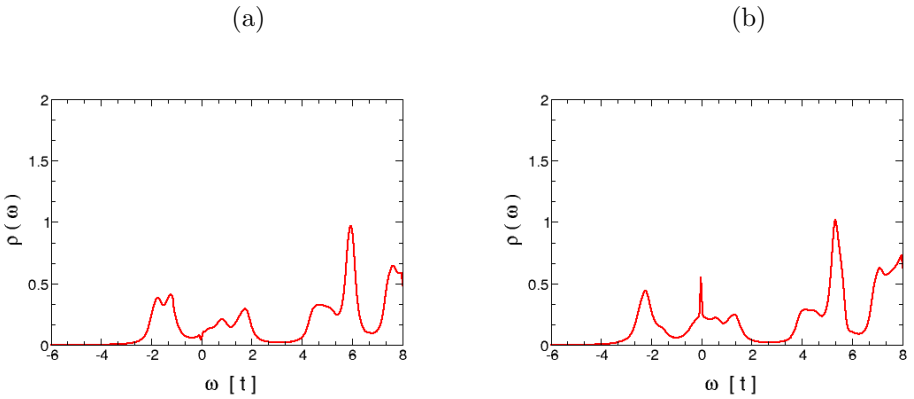

Figure 8.22: The spectral function for the 2x2 tiling with U=10, at densities corresponding to the points at a) $n_{imp} \approx 0.36$ and b) $n_{imp} \approx 0.4$ in Fig 8.20 a).

8.5 Charge Density Distribution

Here we note that we can calculate the real space charge density of the surface states and plot them as in Fig. 8.24 to observe the charge distribution. For example we can consider the 9x9 tiling case at n=0.05 and U=10 shown above in Fig. 8.19 (c), to demonstrate how the distribution of charge changes. At the singular feature below the Fermi level we find that the charge is localised around the impurity, on the three nearest neighbours sites. As we begin to move into the bulk spectral function the charge is predominantly delocalized in the surface states. Deeper into the bulk we find wave like fluctuations in charge density indicative of interactions between localized and itinerant electrons,

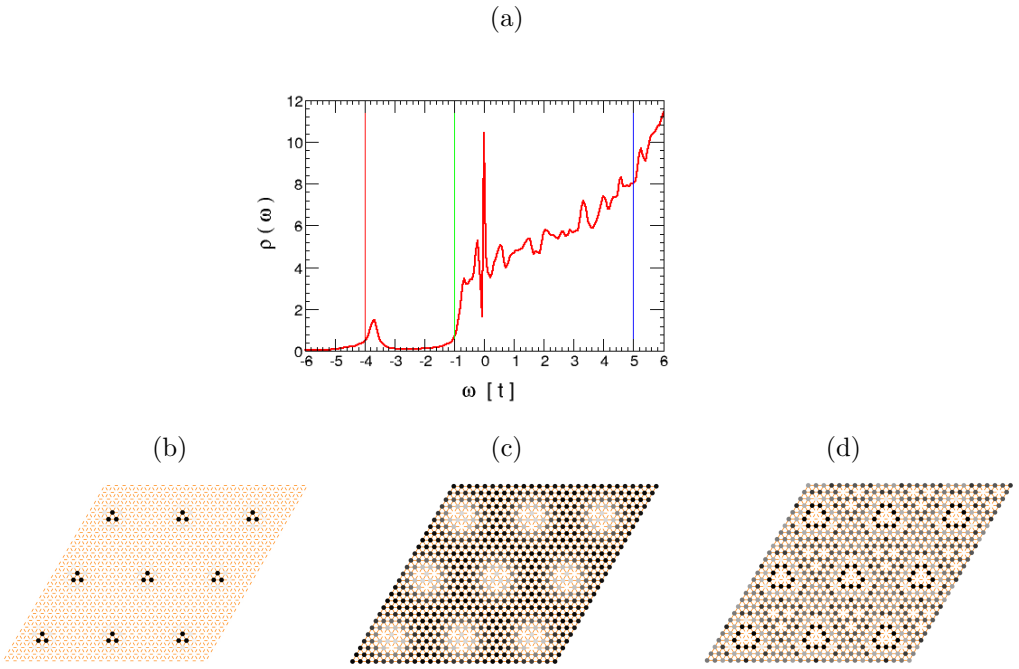

Figure 8.23: a) The spectral function for the 9x9 tile system with U=10 with n=0.05, and the spatially resolved spectral density obtained at energies a) E = -4, b) E = -1 and c) E = 5.

In Fig. 8.24 c) a circular pattern can be seen around the adatom location. This is seen, at all tilings, at energy slices on the edge of the surface spectral function, but its nature becomes clearer when considering the largest tiling of 22x22. This pattern is characteristic of a charge density wave and is due to the presence of the ionic potential, as indicated by its absence when this is set to zero.

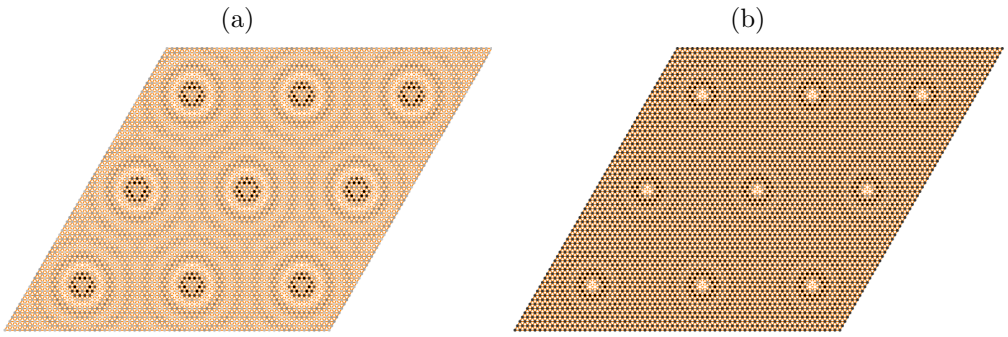

Figure 8.24: The spatially resolved spectral density obtained from a 22x22 tile system with U=10, n=0.005 corresponding to $n_{imp} = 0.5$ shown at an energy slice slightly above the Fermi level just within the surface state spectral function, with a) $V_{Ad} = -3$ and b) $V_{Ad} = 0$.

8.6 Phase diagram of super-lattice systems in the strongly hybridised regime

After giving an overview of the effects of adatom separation and electronic density on several properties we now bring what we have discovered together to connect the different phenomena and identify some particular phases of super-lattice systems. We have chosen to do so using the 2D colour of the Z function at U=10 as the back drop, since this clearly shows the changes in strongly correlated behaviour which we can then overlay with our observations in those regions. In Fig. 8.25 we show the Z function against the impurity density and we overlay this with some regions of other phenomena that have been previously discussed, namely the maximum of the impurity spin and magnetic susceptibility. By considering all of our previous results we have determined the following phases.

Firstly there exists two phases at an impurity density of $n_{imp} \approx 0.3 - 0.4$, which are differentiated by tiling. They both occur for the Z function having a minima near zero, $Z \approx 0$, and also coincide with the maximum impurity spin $S = S_{max}$. At large tilings the magnetic susceptibility is small and as discussed a reduction in this is indicative of Kondo behaviour. At the smallest tilings we also found that the minima of the Z function coincides with zero weight at the Fermi level, $\rho(E_F) = 0$, suggesting charge insulator behaviour (CTI). Increases in tiling from this point cause this system to shift into the Kondo phase and at low tiling these two phases are sensitive

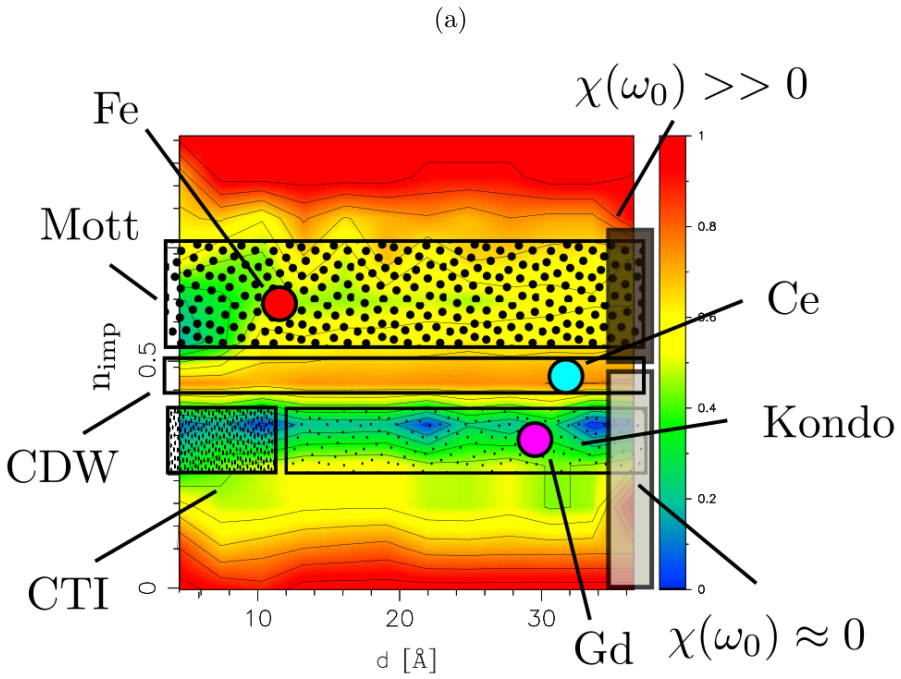

Figure 8.25: The Z function at U=10, with several phases overlaid and identified based on the coincidence of features from numerous properties.

to the impurity occupation.

The central maxima of the Z function denotes what we call a charge density wave (CDW) like phase. We base this on our findings above that at the edge of filling the surface states, just after half filling the impurity, CDW like oscillations can be seen in the spatially resolved spectral densities.

Finally we refer to the second minima of Z as indicative of a Mott-like or correlated metal phase, which coincides also with the maximum of the magnetic susceptibility at large tilings and a similar value at the smallest.

We also indicate the approximate areas where the experimentally observed super-lattices sit, judging by a variety of system parameters shown in Table. 8.1. We place the Ce/Ag(111) system at its corresponding adatom

separation in the central phase corresponding to charge density wave like behaviour. This seems appropriate as the gap opening behaviour of the Ce/Ag(111) system was noted as analogous to CDW [2] which makes it a natural fit here. We place the Gd/Ag(111) in the first strongly correlated region which also corresponds to the maximum impurity spin, again a natural fit since the magnetic moment of Gd is found to be the largest. Finally for the Fe/Cu(111) quasi-super-lattice we place it in the lesser correlated region at a corresponding lower tiling. We judge this sensible since its magnetic moment is slightly reduced to the Ce case which suggest a slightly larger impurity occupation, but this correlated region also appears to persist at U=2 at smaller tilings and the Hubbard U on Fe would be less than that of the lanthanide elements.

Adatom [Substrate]	$r_{\text{ion}}[\mathring{A}]$[86]	μ^a	$d_{\text{Ad-Ad}}[\mathring{A}]$
Ce [Ag(111)]	1.85	2.54	32 [1]
Gd [Ag(111)	2.33	7.94	30 [26]
Fe [Cu(111)]	1.56	2.2	11 [27]

Table 8.1: Observed super-lattices - adatom quantities

[a]Calculated using the Lande g-factor formula

Conclusion

Through our use of dynamical mean field theory to study the behaviour of super-lattices of strongly correlated adatoms on a surface we have determined that the inclusion of the Hubbard U term and its accurate treatment using DMFT, beyond DFT+U methods, is necessary in order to properly understand and describe such systems. We have found clear evidence that a surface hybridising with a strongly correlated impurity is qualitatively different from that just experiencing an ionic potential as previous tight binding models, and consequently our model is much more inclusive of possible super-lattice systems outside of those already exhibiting self assembly which are well described by tight binding.

In particular, our research corroborates the importance of the adatom ionic potential in super-lattice formation, suggesting that when considering strongly correlated adatoms such as Ce, the correspondingly reduced hybridisation between adatom and substrate leaves V_{Ad} as the predominant factor in the Hamiltonian, and the system physics are similar to the original tight binding explanation. Unlike previous work that suggested super-lattice formation for all V_{Ad}, our DMFT treatment shows the importance of the adatom Hubbard U and gives insight into why only a small subset of previously tested adatoms, namely transition and rare earth elements with

localised d or f orbitals, might show this self organising behaviour since for these the strength of the strong correlation is sufficient to suppress hybridisation.

Beyond the inclusion of U we have also studied the effect of system electron density, which represents the element species of the substrate, and adatom-adatom separation on the physics of super-lattice systems, done through consideration of various physical quantities such as impurity occupation, spin and Z. We find a significant breadth of possible physics, borne out of the competition between the many different interactions taken into account. We have observed that the system exhibits strongly correlated behaviour at two impurity occupations, with each being of a different nature, and between them we find a charge density wave like phase.

There are many more aspects of these systems to study, such as the role of magnetism. In this work we did briefly test a cluster DMFT extension, which was alluded to in discussion of our RKKY results. Cluster DMFT is a step back towards the real system, as instead of solving a single impurity problem you solve one with several coupled sites, by having a many-body Green's function and self energy [52] and a correspondingly harder impurity problem to solve. This is a significant improvement as this allow inclusions of RKKY physics, which arise due to many site local interactions which are not captured by H1 or single site DMFT, but is more computationally demanding.

Further work can still be done to look at the case of disorder in the

system, which is a prominent issue in real world systems and could give rise to Anderson localization effects. This would be achieved by considering the many impurity system but allowing random fluctuations in their positions so that they form a slightly disordered lattice. This could be implemented using cluster DMFT by changing the positions of some impurities, but would be particularly computationally expensive, but there is another approach known as molecular DMFT [87]. With this a DMFT loop consists of solving for each impurity sequentially and converging a separate self energy for each. All of these are then incorporated into the Green's function for the next loop, and any differences which arise from different hybridisations due to impurity placements will be passed on.

A goal should also be to perform a full self consistent DFT+DMFT [79] [88] [89] [90] treatment, which will be necessary for true modelling of realistic systems and predictive power. In our investigation we have varied the electronic density and picked adatom Hamiltonian parameters that give qualitative agreement with experiments, but these can easily be replaced with the converged DFT density and parameters gained from a Wannier function description of the adatom's atomic orbitals [91] [92]. The full coupling of DFT and DMFT is not so straightforward however, due to the different mathematical natures of each preventing the simple transfer of information and in particular making isolation of the double counting term difficult [93] [94]. Nevertheless many groups have employed this successfully and much work is being done to add DMFT functionality to black-box

packages (such as FPLO [95][68], ABINIT [96] and CASTEP [97]), which will bring DMFT techniques to the larger community.

In summary our work has corrected a shortfall of previous studies, which could correctly model observed self-assembled super-lattice systems but gave no clear reason for why these systems are so rare. We find that the local strong correlation of lanthanide and possibly transition metal elements is what inhibits hybridisation between bath and impurity, and leaves the system well described by a tight binding Hamiltonian. In addition we find that variations of Hubbard U, adatom separation and electron density in imposed super-lattice systems lead to non-trivial behaviour of impurity characteristics such as spin, Z function and occupation which may well effect the stabilisation of such a structure. While simpler models are sufficient to describe several examples of super-lattice formation, DMFT may be required to further study the myriad interactions that subsequently take place, such as those arising from disorder and magnetic properties.

We hope that our work will contribute to the growing interest around self assembled systems, both in terms of academic research and technological development. We envision that DFT+DMFT simulations built upon the models we have presented here will be key in the discovery of new adatom/-surface combinations that demonstrate this behaviour, and will guide experimental investigations. For their technological potential to be realised a comprehensive description and understanding of strongly correlated, self assembling systems will also be paramount. We have discussed how the field

of magnetic memory storage in particular would benefit greatly from both the ability to fix atomic positions by tuning physical parameters, as opposed to direct manipulation, and the possibility of maintaining distinct magnetic moments at the atomic level thanks to dilute adatom super-lattices. DMFT models will be vital to progress in this area as feasibility of the technology will depend heavily on the impact of magnetic phenomena such as Kondo scattering and the RKKY interaction.

Bibliography

[1] Fabien Silly, Marina Pivetta, Markus Ternes, Fran çois Patthey, Jonathan P. Pelz, and Wolf-Dieter Schneider. Creation of an atomic superlattice by immersing metallic adatoms in a two-dimensional electron sea. *Phys. Rev. Lett.*, 92:016101, Jan 2004. URL: `http://link.aps.org/doi/10.1103/PhysRevLett.92.016101`, `doi:10.1103/PhysRevLett.92.016101`.

[2] Markus Ternes, Cédric Weber, Marina Pivetta, François Patthey, Jonathan P Pelz, Thierry Giamarchi, Frédéric Mila, and Wolf-Dieter Schneider. Scanning-tunneling spectroscopy of surface-state electrons scattered by a slightly disordered two-dimensional dilute "solid": Ce on ag (111). *Physical review letters*, 93(14):146805, 2004.

[3] Chris lutz discusses where moving atoms could take us [online]. URL: `https://www.ibm.com/thought-leadership/innovation_explanations/article/chris_lutz.html`.

[4] Jascha Repp, Francesca Moresco, Gerhard Meyer, Karl-Heinz Rieder, Per Hyldgaard, and Mats Persson. Substrate mediated long-range oscillatory interaction between adatoms: Cu/cu (111). *Physical review letters*, 85(14):2981, 2000.

[5] N Knorr, H Brune, M Epple, A Hirstein, MA Schneider, and K Kern. Long-range adsorbate interactions mediated by a two-dimensional elec-

tron gas. *Physical Review B*, 65(11):115420, 2002.

[6] Stephen Whitelam. Examples of molecular self-assembly at surfaces. *Advanced Materials*, 27(38):5720–5725, 2015.

[7] M Yamagiwa, T Mano, T Kuroda, T Tateno, K Sakoda, G Kido, N Koguchi, and F Minami. Self-assembly of laterally aligned gaas quantum dot pairs. *arXiv preprint cond-mat/0607549*, 2006.

[8] Markus Ternes, Andreas J Heinrich, and Wolf-Dieter Schneider. Spectroscopic manifestations of the kondo effect on single adatoms. *Journal of Physics: Condensed Matter*, 21(5):053001, 2009.

[9] Lihui Zhou, Jens Wiebe, Samir Lounis, Elena Vedmedenko, Focko Meier, Stefan Blügel, Peter H Dederichs, and Roland Wiesendanger. Strength and directionality of surface ruderman–kittel–kasuya–yosida interaction mapped on the atomic scale. *Nature Physics*, 6(3):187–191, 2010.

[10] Sebastian Loth, Susanne Baumann, Christopher P Lutz, DM Eigler, and Andreas J Heinrich. Bistability in atomic-scale antiferromagnets. *Science*, 335(6065):196–199, 2012.

[11] FE Kalff, MP Rebergen, E Fahrenfort, J Girovsky, R Toskovic, JL Lado, J Fernández-Rossier, and AF Otte. A kilobyte rewritable atomic memory. *arXiv preprint arXiv:1604.02265*, 2016.

[12] CY Nakakura, G Zheng, and EI Altman. Atomic-scale mechanisms of the halogenation of cu (100). *Surface science*, 401(2):173–184, 1998.

[13] KH Lau and W Kohn. Indirect long-range oscillatory interaction between adsorbed atoms. *Surface Science*, 75(1):69–85, 1978.

[14] TB Grimley. The indirect interaction between atoms or molecules adsorbed on metals. *Proceedings of the Physical Society*, 90(3):751, 1967.

[15] TB Grimley and SM Walker. Interactions between adatoms on metals and their effects on the heat of adsorption at low surface coverage. *Surface Science*, 14(2):395–406, 1969.

[16] TL Einstein and JR Schrieffer. Indirect interaction between adatoms on a tight-binding solid. *Physical Review B*, 7(8):3629, 1973.

[17] TT Tsong. Field-ion microscope observations of indirect interaction between adatoms on metal surfaces. *Physical Review Letters*, 31(19):1207, 1973.

[18] MS Veshchunov. Indirect interaction between impurity atoms in paramagnetic metals. *Sov. Phys. JETP*, 65(4):835–841, 1987.

[19] E Wahlström, I Ekvall, Håkan Olin, and L Walldén. Long-range interaction between adatoms at the cu (111) surface imaged by scanning tunnelling microscopy. *Applied Physics A: Materials Science & Processing*, 66:1107–1110, 1998.

[20] Philipp Hansmann, Thomas Ayral, Loig Vaugier, Philipp Werner, and Silke Biermann. Long-range coulomb interactions in surface systems: A first-principles description within self-consistently combined g w and dynamical mean-field theory. *Physical review letters*, 110(16):166401, 2013.

[21] Shuyuan Zhang, Hong Zhang, and Yoshiyuki Miyamoto. The inter-adsorbate interaction mediated by shockley-type surface state electrons and dipole moment: Cs and ba atoms absorbed on ag (111) films. *Applied Surface Science*, 289:81–88, 2014.

[22] C Julian Chen. *Introduction to scanning tunneling microscopy*, volume 2. Oxford University Press New York, 1993.

[23] Markus Ternes. *Scanning tunneling spectroscopy at the single atom scale.* PhD thesis, Laboratoire de physique des surfaces SÉCTION DE PHYSIQUE ÉCOLE POLYTECHNIQUE FÉDÉRALE DE LAUSANNE, Technische Universität Berlin, 2006.

[24] NN Negulyaev, VS Stepanyuk, L Niebergall, W Hergert, H Fangohr, and P Bruno. Self-organization of ce adatoms on ag (111): A kinetic monte carlo study. *Physical Review B*, 74(3):035421, 2006.

[25] NN Negulyaev, VS Stepanyuk, L Niebergall, P Bruno, M Pivetta, M Ternes, F Patthey, and W-D Schneider. Melting of two-dimensional adatom superlattices stabilized by long-range electronic interactions. *Physical review letters*, 102(24):246102, 2009.

[26] RX Cao, XP Zhang, BF Miao, ZF Zhong, L Sun, B You, An Hu, and HF Ding. Self-organized gd atomic superlattice on ag (111): Scanning tunneling microscopy and kinetic monte carlo simulations. *Surface Science*, 610:65–69, 2013.

[27] Juanmei Hu, Botao Teng, Fengmin Wu, and Yunzhang Fang. Fe nanostructures stabilized by long-range interactions on cu (111): kinetic monte carlo simulations. *New Journal of Physics*, 10(2):023033, 2008.

[28] XP Zhang, BF Miao, L Sun, CL Gao, An Hu, HF Ding, and J Kirschner. Atomic superlattice formation mechanism revealed by scanning tunneling microscopy and kinetic monte carlo simulations. *Physical Review B*, 81(12):125438, 2010.

[29] Leo Kouwenhoven and Leonid Glazman. Revival of the kondo effect. *arXiv preprint cond-mat/0104100*, 2001.

[30] Ph Nozieres. Some comments on kondo lattices and the mott transition. *The European Physical Journal B-Condensed Matter and Complex Systems*, 6(4):447–457, 1998.

[31] Werner A Hofer, Gilberto Teobaldi, and Nicolas Lorente. Creating pseudo-kondo resonances by field-induced diffusion of atomic hydrogen. *Nanotechnology*, 19(30):305701, 2008.

[32] V Yu Irkhin and AV Zarubin. Metal-insulator transition in the hubbard model: a simple description including the kondo effect. *The Eu-*

ropean Physical Journal B-Condensed Matter and Complex Systems, 38(4):563–570, 2004.

[33] P Wahl, L Diekhöner, MA Schneider, L Vitali, G Wittich, and K Kern. Kondo temperature of magnetic impurities at surfaces. *Physical review letters*, 93(17):176603, 2004.

[34] Philipp Knake and AL Chudnovskiy. Kondo effect and rkky interaction in magnetic trimers. *arXiv preprint arXiv:0905.4392*, 2009.

[35] Philipp Knake. *Interplay of Kondo effect and RKKY interaction in magnetic clusters*. PhD thesis, des Department Physik der Universitat Hamburg, 2010.

[36] Andrew K Mitchell, Dirk Schuricht, Matthias Vojta, and Lars Fritz. Kondo effect on the surface of three-dimensional topological insulators: Signatures in scanning tunneling spectroscopy. *Physical Review B*, 87(7):075430, 2013.

[37] O Újsághy, J Kroha, L Szunyogh, and A Zawadowski. Theory of the fano resonance in the stm tunneling density of states due to a single kondo impurity. *Physical review letters*, 85(12):2557, 2000.

[38] Jozef Spałek and Andrzej Ślebarski. What makes a kondo insulator/semiconductor? In *Journal of Physics: Conference Series*, volume 273, page 012055. IOP Publishing, 2011.

[39] Melvin A Ruderman and Charles Kittel. Indirect exchange coupling of nuclear magnetic moments by conduction electrons. *Physical Review*, 96(1):99, 1954.

[40] Irakli Titvinidze, Andrej Schwabe, Niklas Rother, and Michael Potthoff. Dynamical mean-field theory of indirect magnetic exchange. *Physical Review B*, 86(7):075141, 2012.

[41] Chiung-Yuan Lin, Jheng-Lian Li, Yao-Hsien Hsieh, Keng-Liang Ou, and BA Jones. Magnetic interaction between surface-engineered rare-earth atomic spins. *Physical Review X*, 2(2):021012, 2012.

[42] Lars Hedin, Bengt I Lundqvist, and S Lundqvist. Beyond the one-electron approximation: Density of states for interacting electrons. *Electronic Density of States, NBS Special Publication*, 323:233–249, 1971.

[43] Jiutao Li, Wolf-Dieter Schneider, Richard Berndt, and Bernard Delley. Kondo scattering observed at a single magnetic impurity. *Physical Review Letters*, 80(13):2893, 1998.

[44] NF Mott. Metal-insulator transition. *Reviews of Modern Physics*, 40:677–683, 1968.

[45] Nevill Francis Mott and L Friedman. Metal-insulator transitions in vo2, ti2o3 and ti2-x v x o3. *Philosophical Magazine*, 30(2):389–402, 1974.

[46] PP Edwards, RL Johnston, CNR Rao, DP Tunstall, and F Hensel. The metal–insulator transition: a perspective. *Philosophical Transactions of the Royal Society of London. Series A: Mathematical, Physical and Engineering Sciences*, 356(1735):5–22, 1998.

[47] Rajarshi Tiwari and Pinaki Majumdar. Visualizing the mott transition. *Current Science(Bangalore)*, 103(5):518–524, 2012.

[48] Gabriel Kotliar. The mott transition: Recent results, more surprises [online]. 2002. URL: `http://www.physics.rutgers.edu/~gkguest/papers/kotliar02.pdf`.

[49] Luis Craco and MA Gusmao. From the atomic limit to a metal-insulator transition in the hubbard model. *Physical Review B*, 52(24):17135, 1995.

[50] Antoine Georges, Gabriel Kotliar, Werner Krauth, and Marcelo J. Rozenberg. Dynamical mean-field theory of strongly correlated fermion systems and the limit of infinite dimensions. *Rev. Mod. Phys.*, 68:13–125, Jan 1996. URL: `http://link.aps.org/doi/10.1103/RevModPhys.68.13`, `doi:10.1103/RevModPhys.68.13`.

[51] Andreas Dolfen. *Massively parallel exact diagonalization of strongly correlated systems*. PhD thesis, Diploma Thesis, RWTH Aachen, 2006.

[52] Michael Kinza and Carsten Honerkamp. Two-particle-correlations in dmft (frg). *arXiv preprint arXiv:1307.1298*, 2013.

[53] Walter Kohn and Lu Jeu Sham. Self-consistent equations including exchange and correlation effects. *Physical review*, 140(4A):A1133, 1965.

[54] John C Slater and George F Koster. Simplified lcao method for the periodic potential problem. *Physical Review*, 94(6):1498, 1954.

[55] RT Scalettar. Numerical studies of disordered tight-binding hamiltonians. In *Lectures on the Physics of Strongly Correlated Systems XI(AIP Conference Proceedings Volume 918)*, volume 918, pages 111–202, 2007.

[56] John Hubbard. Electron correlations in narrow energy bands. In *Proceedings of the Royal Society of London A: Mathematical, Physical and Engineering Sciences*, volume 276, pages 238–257. The Royal Society, 1963.

[57] Elliott H Lieb and FY Wu. The one-dimensional hubbard model: a reminiscence. *Physica A: statistical mechanics and its applications*, 321(1):1–27, 2003.

[58] S Akbar Jafari. Introduction to hubbard model and exact diagonalization. *arXiv preprint arXiv:0807.4878*, 2008.

[59] KA Chao, J Spalek, and AM Oles. Kinetic exchange interaction in a narrow s-band. *Journal of Physics C: Solid State Physics*, 10(10):L271, 1977.

[60] J Spalek, AM Oleś, and KA Chao. Effective exchange interactions and magnetic ground state of strongly correlated electrons. *Le Journal de Physique Colloques*, 39(C6):C6–770, 1978.

[61] Jozef Spalek. tj model then and now: a personal perspective from the pioneering times. *arXiv preprint arXiv:0706.4236*, 2007.

[62] Robert Zitzler. *Magnetic Properties of the One-Band Hubbard Model*. PhD thesis, PhD Thesis, Universität Augsburg, 2004.

[63] Philip Warren Anderson. Localized magnetic states in metals. *Physical Review*, 124(1):41, 1961.

[64] Stefan K Kehrein and Andreas Mielke. Theory of the anderson impurity model: The schrieffer–wolff transformation re–examined. *arXiv preprint cond-mat/9510145*, 1995.

[65] Qingguo Feng. *Study of single impurity Anderson model and dynamical mean field theory based on equation-of-motion method*. PhD thesis, der Goethe–Universitat Frankfurt in Frankfurt am Main, 2009.

[66] Sebastian Doniach and Ernst H Sondheimer. *Green's functions for solid state physicists*. Imperial College Press, 1974.

[67] A Avella and D. Vollhardt et al. Mancini, F. *Dynamical Mean Field Theory*, chapter 7. 2011.

[68] Erik Ryan Ylvisaker. *DFT and DMFT: Implementations and Applications to the Study of Correlated Materials*. University of California, Davis, 2008.

[69] Walter Metzner and Dieter Vollhardt. Correlated lattice fermions in $d = \infty$ dimensions. *Phys. Rev. Lett.*, 62:1066–1066, Feb 1989. URL: `http://link.aps.org/doi/10.1103/PhysRevLett.62.1066.2`, `doi:10.1103/PhysRevLett.62.1066.2`.

[70] André-Marie Tremblay. A refresher in many-body theory [online]. 2008. URL: `http://www.physique.usherbrooke.ca/tremblay/cours/phy-892/jouvence.pdf`.

[71] Richard D Mattuck. *A guide to Feynman diagrams in the many-body problem*. Courier Corporation, 2012.

[72] C Weber, A Amaricci, M Capone, and PB Littlewood. Augmented hybrid exact-diagonalization solver for dynamical mean field theory. *Physical Review B*, 86(11):115136, 2012.

[73] John Hubbard. Electron correlations in narrow energy bands. iii. an improved solution. In *Proceedings of the Royal Society of London A: Mathematical, Physical and Engineering Sciences*, volume 281, pages 401–419. The Royal Society, 1964.

[74] Hans Rademacher. On the partition function p (n). *Proceedings of the London Mathematical Society*, 2(1):241–254, 1938.

[75] Li Huang, Tim O Wehling, and Philipp Werner. Electronic excitation spectra of the five-orbital anderson impurity model: From the atomic limit to itinerant atomic magnetism. *Physical Review B*, 89(24):245104, 2014.

[76] Sahana Murthy. *Mott transition in strongly correlated materials: a realistic modeling using LDA+ DMFT*. PhD thesis, Rutgers, The State University of New Jersey, 2004.

[77] Eva Pavarini, Erik Koch, Dieter Vollhardt, and Alexander Lichtenstein. *DMFT at 25: Infinite Dimensions: Lecture Notes of the Autumn School on Correlated Electrons 2014*, volume 4. Forschungszentrum Jülich, 2014.

[78] Brigitte Surer. *First-principles simulations of multi-orbital systems with strong electronic correlations*. PhD thesis, Diss., Eidgenössische Technische Hochschule ETH Zürich, Nr. 19902, 2011.

[79] LV Pourovskii, B Amadon, S Biermann, and A Georges. Self-consistency over the charge density in dynamical mean-field theory: A linear muffin-tin implementation and some physical implications. *Physical Review B*, 76(23):235101, 2007.

[80] Cédric Weber, Kristjan Haule, and Gabriel Kotliar. Apical oxygens and correlation strength in electron-and hole-doped copper oxides. *Physical Review B*, 82(12):125107, 2010.

[81] William W Hager. Updating the inverse of a matrix. *Society for Industrial and Applied Mathematics (SIAM) Review*, 31(2):221–239, 1989.

[82] Gene H Golub and Charles F Van Loan. *Matrix computations*, volume 3. JHU Press, 2012.

[83] Yoyo Hinuma, Giovanni Pizzi, Yu Kumagai, Fumiyasu Oba, and Isao Tanaka. Band structure diagram paths based on crystallography. *Computational Materials Science*, 128:140–184, 2017.

[84] Rajdeep Sensarma, EH Hwang, and S Das Sarma. Quasiparticles, plasmarons, and quantum spectral function in bilayer graphene. *Physical Review B*, 84(4):041408, 2011.

[85] Ralph Skomski, R Zhang, P Kharel, Axel Enders, S-H Liou, and David J Sellmyer. Magnetic susceptibility of nanoscale kondo systems. *Journal of Applied Physics*, 107(9):09E126, 2010.

[86] E t Clementi and D-L_ Raimondi. Atomic screening constants from scf functions. *The Journal of Chemical Physics*, 38(11):2686–2689, 1963.

[87] Dominika Zgid and Garnet Kin-Lic Chan. Dynamical mean-field theory from a quantum chemical perspective. *The Journal of chemical physics*, 134:094115, 2011.

[88] AK McMahan. Combined local-density and dynamical mean field theory calculations for the compressed lanthanides ce, pr, and nd. *Physical Review B*, 72(11):115125, 2005.

[89] B Amadon. A self-consistent dft+ dmft scheme in the projector augmented wave method: applications to cerium, ce2o3 and pu2o3 with the hubbard i solver and comparison to dft+ u. *Journal of Physics: Condensed Matter*, 24(7):075604, 2012.

[90] Zhao Jian-Zhou, Zhuang Jia-Ning, Deng Xiao-Yu, Bi Yan, Cai Ling-Cang, Fang Zhong, and Dai Xi. Implementation of lda+ dmft with the pseudo-potential-plane-wave method. *Chinese Physics B*, 21(5):057106, 2012.

[91] Gregory H Wannier. The structure of electronic excitation levels in insulating crystals. *Physical Review*, 52(3):191, 1937.

[92] Franck Lechermann, A Georges, A Poteryaev, S Biermann, M Posternak, A Yamasaki, and OK Andersen. Dynamical mean-field theory using wannier functions: A flexible route to electronic structure calculations of strongly correlated materials. *Physical Review B*, 74(12):125120, 2006.

[93] Hung Dang. Double counting in the density functional plus dynamical mean-field theory of transition metal oxides. In *APS Meeting Abstracts*, volume 1, page 32004, 2015.

[94] Hung T Dang, Xinyuan Ai, Andrew J Millis, and Chris A Marianetti. Density functional plus dynamical mean-field theory of the metal-insulator transition in early transition-metal oxides. *Physical Review B*, 90(12):125114, 2014.

[95] Fplo: full-potential local-orbital package [online]. URL: `http://www.fplo.de/`.

[96] Xavier Gonze, François Jollet, F Abreu Araujo, Donat Adams, Bernard Amadon, Thomas Applencourt, Christophe Audouze, J-M Beuken, Jordan Bieder, A Bokhanchuk, et al. Recent developments in the abinit software package. *Computer Physics Communications*, 205:106–131, 2016.

[97] Strong correlation meets materials modelling: Dmft and gw in castep [online]. URL: `http://gow.epsrc.ac.uk/NGBOViewGrant.aspx?GrantRef=EP/M010953/1`.